Membrane binding properties of the cytoskeletal protein bactofilin

Ying Liu[1,#], Rajani Karmakar[2], Wieland Steinchen[3,4], Saumyak Mukherjee[2], Gert Bange[3,4,5], Lars V. Schäfer[2], Martin Thanbichler[1,4,6*]

[1] Department of Biology, University of Marburg, 35032 Marburg, Germany
[2] Theoretical Chemistry, Ruhr University Bochum, 44780 Bochum, Germany
[3] Department of Chemistry, University of Marburg, 35032 Marburg, Germany
[4] Center for Synthetic Microbiology (SYNMIKRO), 35032 Marburg, Germany
[5] Max Max Planck Fellow Group Molecular Physiology of Microbes, Max Planck Institute for Terrestrial Microbiology, 35043 Marburg, Germany
[6] Max Planck Fellow Group Bacterial Cell Biology, Max Planck Institute for Terrestrial Microbiology, 35043 Marburg, Germany

[#] Present address: Universitätsklinikum Schleswig-Holstein, 24105 Kiel, Germany

*Address correspondence to
Martin Thanbichler (thanbichler@uni-marburg.de)

Keywords
Cytoskeletal protein, bactofilin, CcmA, membrane-targeting sequence, membrane binding

Abstract

Bactofilins are a widespread family of cytoskeletal proteins with important roles in bacterial morphogenesis, chromosome organization and motility. They polymerize in a nucleotide-independent manner, forming non-polar filaments that are typically associated with the cytoplasmic membrane. Membrane binding was suggested to be mediated by a short N-terminal peptide, but the underlying mechanism and the conservation of this interaction determinant among bacteria remain unclear. Here, we use the bactofilin homolog BacA of the stalked bacterium *Caulobacter crescentus* as a model to analyze the membrane-binding behavior of bactofilins. Based on site-directed mutagenesis of the N-terminal region, we identify the full membrane-targeting sequence of BacA (MFSKQAKS) and identify amino acid residues that are critical for its function *in vivo* and *in vitro*. Molecular dynamics simulations then provide detailed insight into the molecular mechanism underlying the membrane affinity of this peptide. Collectively these analyses reveal a delicate interplay between the water exclusion of hydrophobic N-terminal residues, the arrangement of the peptide within the membrane and the electrostatic attraction between positively charged groups in the peptide and negative charges in the phospholipid molecules. A comprehensive bioinformatic analysis shows that the composition and properties of the membrane-targeting sequence of BacA are conserved in numerous bactofilin homologs from diverse bacterial phyla. Notably, our findings reveal a mutual interdependence between the membrane binding and polymerization activities of BacA. Moreover, we demonstrate that both of these activities have a pivotal role in the recruitment of the BacA client protein PbpC, a membrane-bound cell wall synthase involved in stalk formation whose N-terminal region turns out to associate with the core polymerization domain of BacA. Together, these results unravel the mechanistic underpinnings of membrane binding by bactofilin homologs, thereby illuminating a previously obscure but important aspect in the biology of this cytoskeletal protein family.

Introduction

22 Cytoskeletal proteins mediate a variety of fundamental cellular processes in bacteria, including cell growth,
23 cell division and DNA segregation (Cabeen and Jacobs-Wagner, 2010; Wagstaff and Löwe, 2018). Many
24 important components of the bacterial cytoskeleton have eukaryotic homologs. The conserved cell divi-
25 sion protein FtsZ, for instance, is a member of the tubulin superfamily (Löwe and Amos, 1998; Mukherjee
26 et al., 1993), forming dynamic polymers at the cell division site that control the assembly and function of
27 the cell division apparatus (McQuillen and Xiao, 2020). The morphogenetic protein MreB, by contrast,
28 which governs cell growth and morphology in most rod-shaped bacteria (Jones et al., 2001; van den Ent
29 et al., 2001), is homologous to actin (Rohs and Bernhardt, 2021). In addition, bacteria also contain inter-
30 mediate-filament-like proteins, such as the coiled-coil-rich protein crescentin, which promotes cell curva-
31 ture in the crescent-shaped alphaproteobacterium *Caulobacter crescentus* (Ausmees et al., 2003; Liu et
32 al., 2024). Apart from these universally conserved cytoskeletal protein families, bacteria contain a variety
33 of polymer-forming proteins that are typically absent from eukaryotes (Wagstaff and Löwe, 2018). A
34 prominent member of this group of proteins is bactofilin (Kühn et al., 2010).

35 Bactofilin homologs are widespread among bacteria and involved in diverse cellular functions. In many
36 species, they have important roles in cell shape determination, including the establishment or adjustment
37 of cell curvature in *Helicobacter pylori* (Sycuro et al., 2010), *Campylobacter jejuni* (Frirdich et al., 2023),
38 *Leptospira biplexa* (Jackson et al., 2018) and *Rhodospirillum rubrum* (Pöhl et al., 2024), the modulation of
39 cell size in *Chlamydia trachomatis* (Brockett et al., 2021), the formation of buds in *Hyphomonas neptunium*
40 (Pöhl et al., 2024), the stabilization of rod shape in *Myxococcus xanthus* (Koch et al., 2011) and *Proteus*
41 *mirabilis* (Hay et al., 1999) and the synthesis of stalk-like cellular extensions in *C. crescentus* (Kühn et al.,
42 2010), *Asticcacaulis biprosthecum* (Caccamo et al., 2020) and *Rhodomicrobium vannielii* (Richter et al.,
43 2023). Other functions include DNA organization in *M. xanthus* (Anand et al., 2020; Lin et al., 2017) as well
44 as cell motility in *Bacillus subtilis* (El Andari et al., 2015). Bactofilins are relatively small proteins charac-
45 terized by a central Bactofilin A/B domain (InterPro ID: IPR007607) that is typically flanked by unstructured
46 terminal regions of varying lengths. The central domain is ~110 amino acids long and folds into a compact
47 right-handed β-helix with a triangular geometry, measuring roughly 3 nm along its longitudinal axis
48 (Kassem et al., 2016; Shi et al., 2015; Vasa et al., 2015; Zuckerman et al., 2015). This basic unit polymerizes
49 into extended non-polar filaments through alternating head-to-head and tail-to-tail interactions between
50 individual subunits (Deng et al., 2019). The resulting protofilaments can further assemble into higher-
51 order structures such as bundles, lattices and 2D crystalline sheets *in vitro* (Holtrup et al., 2019; Kühn et

52 al., 2010; Pöhl et al., 2024; Sichel et al., 2022; Vasa et al., 2015; Zuckerman et al., 2015) and, potentially,
53 also *in vivo* (Kühn et al., 2010). Previous studies have indicated that bactofilins are typically associated
54 with the cytoplasmic membrane (Deng et al., 2019; Hay et al., 1999; Koch et al., 2011; Kühn et al., 2010;
55 Lee et al., 2023). However, only a small subset of them, including certain gammaproteobacterial represen-
56 tatives (Hay et al., 1999), contain predicted transmembrane helices, suggesting that canonical bactofilins
57 use an unconventional membrane-targeting mechanism that may have specifically evolved in this cyto-
58 skeletal protein family. Consistent with this notion, the membrane-binding activity of bactofilin homologs
59 from *Thermus thermophilus* (Deng et al., 2019) and *C. trachomatis* (Lee et al., 2023) has recently been
60 shown to depend on a short peptide in the N-terminal unstructured region of the proteins. However, the
61 conservation of this peptide, the precise mechanism underlying its affinity for the lipid bilayer, and the
62 interplay between membrane attachment and bactofilin polymerization still remain to be investigated.

63 In this study, we comprehensively analyze the membrane-binding behavior of bactofilins, using BacA from
64 *C. crescentus* as a model protein. Previous work has shown that BacA forms membrane-associated poly-
65 meric sheets at the old pole of the *C. crescentus* cell, which recruit the cell wall synthase PbpC to stimulate
66 stalk formation at this subcellular location (Billini et al., 2019; Hughes et al., 2013; Kühn et al., 2010). By
67 systematically exchanging residues in the N-terminal region of BacA, we identify a short N-terminal pep-
68 tide (MFSKQAKS) that acts as the membrane-targeting sequence (MTS) of BacA and pinpoint residues
69 critical for its membrane-binding activity *in vivo* and *in vitro*. We then clarify the molecular mechanism
70 underlying the membrane affinity of this sequence using molecular dynamics simulations. A compre-
71 hensive bioinformatic analysis suggests that the mode of action revealed for the MTS of BacA is conserved
72 in a large number of bactofilin homologs from various different phyla. Importantly, our findings indicate
73 a mutual stimulatory effect of BacA membrane association and polymerization as well as a key role of
74 BacA assembly in the interaction with its client protein PbpC. Together, these findings reveal the mecha-
75 nistic basis of membrane binding by bactofilin homologs and highlight the implications of this process for
76 bactofilin function, thereby shedding light on a thus-far poorly understood aspect in the biology of this
77 widespread cytoskeletal protein.

Results

78 **The membrane-binding activity of BacA depends on an N-terminal amphipathic peptide**

79 Previous work has proposed a small N-terminal peptide as the membrane-targeting sequence (MTS) of
80 canonical bactofilin homologs (Deng et al., 2019). In the case of *C. crescentus* BacA, the suggested region
81 comprises the sequence MFSKQAKS at the N-terminal end of the protein (**Figure 1A**). To verify the impor-
82 tance of this peptide for BacA function, we compared the localization pattern of wild-type BacA with that
83 of a mutant derivative lacking the predicted membrane-targeting sequence (MTS). For this purpose, the
84 two proteins were fused to the monomeric yellow fluorescent protein mVenus and produced in a strain
85 carrying an in-frame deletion in the endogenous *bacA* and *bacB* genes (**Figure 1B**). As expected, the wild-
86 type protein was fully functional and formed distinct fluorescent foci at the stalked pole of the cells, which
87 have been previously shown to reflect the formation of small patches of membrane-associated BacA
88 polymers (Kühn et al., 2010). The mutant protein (Δ2-8), by contrast, was evenly distributed in the cyto-
89 plasm, supporting a role of the N-terminal region of BacA in membrane binding. The diffuse localization
90 also suggests a defect in polymerization, which however may be a secondary effect resulting from the loss
91 of membrane association, since previous work has shown that the unstructured terminal regions are not
92 essential for bactofilin assembly (Sichel et al., 2022; Vasa et al., 2015). Notably, an amino acid exchange
93 that disrupted the C-terminal polymerization interface of the Bactofilin A/B domain (F130R) (Deng et al.,
94 2019; Vasa et al., 2015; Zuckerman et al., 2015) also led to an even distribution of BacA-mVenus within
95 the cell (**Figure 1B**), supporting the idea that polymerization and membrane binding are mutually inter-
96 dependent.

97 Apart from transmembrane segments, proteins commonly employ amphiphilic helices to associate with
98 the inner face of the cytoplasmic membrane, as exemplified by the bacterial actin homologs FtsA (Pichoff
99 and Lutkenhaus, 2005) and MreB (Salje et al., 2011). As a first step to clarify the mechanism underlying
100 the membrane-binding activity of the MTS, we therefore determined whether it was able to adopt an
101 amphiphilic helical structure. However, neither machine-learning-based pattern recognition, as employed
102 by AmphipaSeek (Sapay et al., 2006) (**Figure 1A**), nor helical wheel analysis (**Figure 1C**) provided any sup-
103 port for this possibility, suggesting a different mode of action.

104 To obtain more insight into the function of the MTS, we went on to systematically exchange single or
105 multiple amino acid residues in the N-terminal eight amino acids of BacA-mVenus (**Figure S1**) and analyze
106 the localization patterns of the mutant proteins. Among the single exchanges, substitution of the hydro-
107 phobic phenylalanine residue at position 2 (F2Y and F2E) led to a disperse or, occasionally, patchy distribu-

108 tion of the fusion protein (**Figure 1B**). Other single substitutions, by contrast, had relatively mild effects,
109 including the formation of multiple and/or mispositioned bactofilin complexes (**Figure S2**). Notably, how-
110 ever, a double exchange replacing the two positively charged lysine residues in the MTS with polar serine
111 residues (K4S-K7S) strongly increased the fraction of delocalized protein (**Figure 1B**), although distinct
112 fluorescent foci or patches were still detectable, indicating residual membrane-binding activity. An even
113 stronger effect, as reflected by a complete dispersion of the fluorescence signal, was observed when nega-
114 tively charged glutamate residues were introduced at these positions (K4E-K7E). Collectively, these results
115 point to a central role of F2 and K4/K7 in the association of BacA with the cytoplasmic membrane.

116 To further characterize the mutant BacA-mVenus variants, we analyzed their mobility within the cell using
117 single-particle tracking (**Figure 2A**). As expected by its ability to interact with the membrane and poly-
118 merize, the wild-type protein exhibited a very low diffusional mobility. Mutant variants that were partially
119 delocalized (F2Y and K4S-K7S) were significantly more mobile, and variants with an entirely diffuse localiz-
120 ation (Δ2-8, F2E, K4E-K7E and F2E-K4E-K7E) displayed the highest diffusion rates. These results support
121 the notion that the MTS is required for the formation of stable membrane-associated BacA assemblies.

122 As a direct means to analyze the membrane-binding activity of the fusion proteins, we next performed
123 cell fractionation studies. To this end, cells producing different BacA-mVenus variants were lysed and
124 membranes were separated from soluble components by ultracentrifugation. Western blot analysis re-
125 vealed that a large part of the wild-type protein was detected in the membrane fraction, whereas the
126 variant lacking the MTS (Δ2-8) was completely soluble (**Figure 2B**). A severe reduction in membrane-
127 binding activity was also observed for all fusion proteins lacking residues F2 and K4/K7 (**Figure 2C**), con-
128 firming the importance of these residues in the function of the MTS.

129 After having identified a role of the MTS in the association of BacA with membranes *in vivo*, we aimed to
130 verify the membrane-targeting activity of this peptide in a defined system *in vitro*. For this purpose, we
131 purified wild-type BacA and various mutant derivatives, using a cleavable N-terminal His_6-SUMO affinity
132 tag (Marblestone et al., 2006), which allowed us to obtain proteins without any non-native extensions
133 that could potentially interfere with the analysis. This approach also made it possible to obtain two addi-
134 tional BacA variants, one lacking the N-terminal methionine of BacA (ΔM) and another one lacking the N-
135 terminal methionine and containing a glutamate instead of the phenylalanine normally located at the
136 second position of the MTS (xE). We then incubated the different proteins with small unilamellar vesicles
137 (liposomes) made of phosphatidylglycerol, which has been identified as the most abundant membrane
138 lipid in *C. crescentus* under standard growth conditions (Contreras et al., 1978; Stankeviciute et al., 2019).

139 Subsequently, the liposomes were collected by ultracentrifugation and analyzed for the amount of bound
140 protein (**Figure 3**). Consistent with the *in vivo* data, a large proportion (~80%) of the wild-type protein was
141 associated with the liposome pellet, whereas only a small fraction sedimented in control reactions lacking
142 liposomes, likely reflecting large, poorly soluble polymer bundles. Removal of the entire MTS and an ex-
143 change of residues F2 or K4/K7 again caused a severe defect in membrane binding, reducing the sedimen-
144 tation efficiencies to those obtained in the liposome-free control reactions. The lack of residue M1 (ΔM),
145 by contrast, only caused a moderate reduction in the membrane-binding activity of BacA, indicating that
146 it plays a significant but not decisive role in the function of the MTS (**Figure 3**). Together, these results
147 verify the existence of an N-terminal MTS in BacA. Moreover, they identify the N-terminal hydrophobic
148 residues M1 and F2 and the two positively charged lysine residues K4 and K7 as key determinants of its
149 membrane-binding affinity.

150 **BacA polymerization and membrane binding are mutually interdependent**

151 Our results showed that the disruption of the polymerization interface (F130R) resulted in a diffuse, cyto-
152 plasmic localization of BacA, suggesting that polymerization might be a prerequisite for efficient mem-
153 brane binding (**Figure 1C**). To investigate this possibility, we clarified the membrane-binding activity of the
154 polymerization-deficient F130R variant of BacA-mVenus. Cell fractionation experiments showed that the
155 fusion protein was barely detectable in the membrane fraction (**Figure 4A**). In line with this finding, only
156 marginal membrane-binding activity was observed for the untagged BacA-F130 variant in liposome-bind-
157 ing assays (**Figure 4B**). These results suggest that the MTS has a relatively low affinity for the membrane,
158 so that a stable interaction can only be achieved by cooperative binding of multiple MTS-containing N-
159 terminal tails, arrayed on the surface of bactofilin polymers. Further support for this idea came from do-
160 main swapping experiments that showed that the MTS of BacA was able to mediate stable membrane
161 attachment when fused to a derivative of the polymer-forming protein crescentin from *C. crescentus* lack-
162 ing its native membrane-targeting sequence (**Figure S3**).

163 Interestingly, the diffuse localization and high diffusional mobility of BacA variants containing a defective
164 MTS (**Figures 1C and 2A**) indicate that there may also be a converse stimulatory effect of membrane bind-
165 ing on BacA polymerization. To further assess this possibility, we analyzed whether an MTS-defective BacA
166 variant could regain the ability to form membrane-associated polymeric complexes if equipped with a
167 heterologous membrane-targeting sequence. To this end, two copies of the N-terminal amphiphilic helix
168 of MreB from *E. coli* (Salje et al., 2011) were fused to a BacA-mVenus variant lacking the native MTS-
169 containing peptide (Δ2-8). Microscopic analysis revealed that the fusion protein condensed into distinct

170 foci at the old pole or the cell center (**Figure 4C**), reminiscent of the aberrant localization patterns ob-
171 served for mutant proteins with exchanges in the MTS that did not completely abolish membrane binding
172 (compare **Figure S2**). The restoration of fluorescent foci was accompanied by a strong decrease in diffu-
173 sional mobility, as determined by single-molecule tracking (**Figure 4D**). In addition, cell fractionation ex-
174 periments showed that the fusion protein was highly enriched in the membrane pellet (**Figure 4E**). Im-
175 portantly, when its polymerization interface was disrupted by introduction of the F130R exchange, focus
176 formation was abolished, membrane binding was strongly reduced, and the diffusional mobility of the
177 fusion protein increased to a value similar to that of an F130R variant containing the native MTS of BacA
178 (**Figure 4C-E**). Collectively, these findings demonstrate that the polymerization and membrane-binding
179 activities of BacA strongly stimulate each other.

180 **Molecular dynamics simulations identify M1, K4 and K7 as key residues of the BacA MTS**

181 To investigate the molecular underpinnings of the interaction between the MTS of BacA and the mem-
182 brane, we turned to all-atom molecular dynamics (MD) simulations. For this purpose, peptides comprising
183 the ten N-terminal bactofilin residues were simulated in the presence of a multi-component lipid bilayer
184 that was composed of approxiamtely 50% monoglucosyldiglyceride (GLY), 33% phosphatidylglycerol (PG)
185 and 16% diacylglycerol (DAG) lipids (see **Table S1** for details), approximating the native composition of
186 *C. crescentus* cell membranes under standard growth conditions (Chow and Schmidt, 1974; Contreras et
187 al., 1978; Stankeviciute et al., 2019). In addition to the wild-type peptide MFSKQAKSNN, our analysis also
188 included the mutant F2Y and K4S-K7S variants (each in a separate simulation).

189 The starting structures of the peptides were modeled in an extended conformation without any secondary
190 structure. At the beginning, a single peptide (wild-type, F2Y or K4S-K7S) was placed in the aqueous phase
191 at a distance of ca. 3 nm from the lipid headgroups. During the 500-ns simulations, all three peptides
192 rapidly bound to the membrane and established multiple contacts with the lipids at the membrane/water
193 interface (**Figure 5A**). In doing so, the peptides did not adopt any persistent secondary structures but
194 remained disordered, with a preference for somewhat extended conformations (**Figure 5B,C**). Notably, in
195 control simulations in which the peptides were initially modeled as α-helices, the peptides unfolded rapid-
196 ly, either in the aqueous phase or after binding to the membrane/water interface, eventually yielding the
197 same results (within the statistical uncertainties) as the simulations starting from an extended conforma-
198 tion.

199 Excluding the initial phase of the simulations in which the peptides were not yet bound to the membrane,
200 we then determined the density profiles of the three different peptides along the membrane normal

201 (**Figures 5D and S4**). The results show that the N-terminal residues 1 and 2 insert deeply into the lipid
202 bilayer, assuming positions below the phosphate headgroup region, while the positions of the remaining
203 residues (3 to 10) are gradually shifted towards the aqueous phase. The peptides thus bind to the mem-
204 brane in a tilted orientation, with their N-terminal region protruding more deeply into the hydrophobic
205 parts of the lipid headgroup region (**Figure 5B**). Interestingly, in case of the F2Y variant, the presence of
206 tyrosine at position 2 pulls residue M1 and Y2 further towards the headgroup/water interface (**Figure S4B**).
207 This result can be explained by the preferential hydration of tyrosine compared to phenylalanine, as is
208 also reflected in the difference of the solvation free energies (ΔG_{solv}) of the corresponding side-chain
209 analogs *p*-cresol (-25.6 kJ mol^{-1}) and toluene (-3.2 kJ mol^{-1}) (Wolfenden et al., 1981).

210 To characterize the interactions between the peptides and the membrane in more detail, the contacts
211 between the individual peptide residues and the different lipid species in the bilayers were counted. The
212 results confirm the above finding that residues 1 and 2 show the strongest association with lipids and that
213 lipid interactions gradually decrease for residues further down the peptide chain (**Figure 6A**). Notably,
214 among these interactions, contacts with anionic PG lipids dominate, even though the percentage of PG
215 lipids (33%) in the simulated bilayer is smaller than that of GLY lipids (50%) (see above and **Table S1**),
216 which can largely be attributed to the lysine residues at positions 4 and 7. In line with this result, the K4S-
217 K7S variant shows a strong reduction in the number of PG contacts at these positions, which is partially
218 compensated by a higher prevalence of GLY contacts, particularly for residues 1 to 5 (**Figure 6A**). The F2Y
219 variant, by contrast, did not show a marked decrease in the number of total lipid contacts for position 2,
220 with fewer PG contacts (of residues 1 and 2) again compensated by more GLY lipid contacts (**Figure 6A**).
221 Taken together, the lipid contact analysis shows that the N-terminal residues M1 and F2 establish the
222 closest contacts with the lipid bilayer, and that the lysine residues K4 and K7 strongly interact with PG
223 lipids.

224 The contact analysis described above only provides insight into the spatial proximity of the peptides and
225 the lipids. To additionally determine the strength of the interactions, we analyzed the MD simulations in
226 terms of the interaction energies between the different peptide residues and the lipid molecules (**Figure**
227 **6B**). For both the wild-type peptide and its F2Y variant, the strongest (most favorable) peptide-lipid inter-
228 action energy is seen for residues 1, 4 and 7, which can be attributed to strong electrostatic attraction
229 between the PG lipids and the charged NH_3^+ group at the N-terminus (residue M1) as well as the side
230 chains of residues K4 and K7, respectively. Notably, out of all residues, M1 interacts most strongly with
231 the membrane. However, its removal (ΔM) had only a moderate effect on the membrane-binding activity
232 of BacA *in vitro* (**Figure 3**), corroborating the notion that the largest part of the interaction energy is

233 provided by the N-terminal NH_3^+ group of M1 rather than its hydrophobic side chain. However, taken
234 together, the two lysines K4 and K7 make an even larger contribution to the interaction, which is in line
235 with the complete loss of membrane association observed for the K4S-K7S variants of BacA (**Figures 1C,**
236 **2C and 3**). It is interesting to note that in terms of the interaction energy, residue F2 does not seem to
237 play a prominent role in the peptide-membrane association (**Figure 6B**), although the F2Y exchange
238 strongly reduces the membrane-binding affinity of BacA *in vivo* and, even more so, *in vitro* (**Figures 1C, 2C**
239 **and 3**). The deleterious effect of this exchange may be explained by the preferential hydration of tyrosine
240 compared to phenylalanine, which is not reflected in the peptide-membrane interaction energy but in the
241 difference in hydration free-energy (see above). Furthermore, residues M1 and Y2 in the F2Y peptide are
242 located in closer proximity to the aqueous phase (see **Figure S4B**), which leads to a substantial decrease
243 in the favorable interaction energy of the N-terminal NH_3^+-group with PG lipids that is only incompletely
244 compensated by slightly more favorable interactions with GLY lipids (**Figure 6B**). Together, these results
245 provide a rational basis for the experimental finding that the F2Y and K4S-K7S variants of BacA have a
246 considerably lower membrane-binding affinity than the wild-type protein.

247 **The N-terminal membrane-targeting sequence is conserved among bactofilin homologs**

248 The results of the MD simulations confirmed that the short peptide (MFSKQAKS) at the N-terminus of
249 BacA acts as an MTS. To assess whether this mode of interaction was more widespread among bactofilins,
250 we set up a bioinformatic pipeline to analyze the conservation of the N-terminal region of bactofilin homo-
251 logs from a broad range of bacterial lineages (**Figure S5**). To this end, all proteins containing an annotated
252 bactofilin domain were retrieved from the UniProt database (UniProt Consortium, 2023). After the exclu-
253 sion of entries from non-bacterial origin, we eliminated all bactofilin homologs containing predicted N-
254 terminal transmembrane helices as a membrane anchor. These proteins were relatively rare (~3.2%) but
255 widely distributed across the bacterial phylogeny, with the majority found in the gammaproteobacteria
256 (**Figure S5**). To account for biases in the coverage of bacterial species, we next filtered out homologs with
257 highly similar amino acid sequences. For each of the remaining proteins, we then determined the N-
258 terminal region preceding the bactofilin domain. Based on the length of the MTS identified for BacA, we
259 eliminated proteins whose predicted N-terminal tails were shorter than this minimal length, potentially
260 due to misannotation of the translational start sites. The remaining proteins (14337) were then used to
261 search for conserved N-terminal amino acid motifs.

262 A global analysis of the entire protein set yielded a conserved motif with the consensus sequence
263 MFSKKKK, which resembled the MTS identified for *C. crescentus* BacA and contained both the two hydro-

264 phobic N-terminal residues that insert into the core of the lipid bilayer as well as the two lysin residues
265 that make electrostatic interactions with the headgroups of PG lipids (**Figure 7**). This result suggests that
266 the presence of an N-terminal MTS is a common feature of bacterial bactofilin homologs. However, this
267 global approach might obscure lineage-specific adaptations of the MTS to evolutionary differences in
268 membrane lipid composition. To address this issue, we conducted an additional analysis in which we sort-
269 ed the proteins according to their phylogenetic origin before performing a motif search. In doing so, we
270 focused on the phyla Pseudomonadota, Bacteroidota, Bacillota, Spirochaetota and Thermodesulfobac-
271 teriota, which contribute the majority of the bactofilin homologs in the UniProt database. This refined
272 analysis confirmed the presence of conserved N-terminal motifs in each of the five phyla, although there
273 is variability in the consensus sequences of these motifs both within and between phyla (**Figure S6**). A
274 comparison of the most abundant motifs (**Figure 7**) revealed that bactofilin homologs from Pseudomona-
275 dota and Bacillota share highly similar N-terminal sequences, which largely correspond to the global motif
276 described above. A similar N-terminal motif is also found in most bactofilin homologs from Bacteroidota,
277 although these proteins often display a negatively rather than a positively charged residue at position 4.
278 The motifs identified for Spirochaetota and Thermodesulfobacteriota, by contrast, have fundamentally
279 different consensus sequences, likely reflecting a different mode of membrane binding (**Figures 7 and S6**).
280 Together, these results strongly suggest that the majority of bactofilin homologs known to date feature
281 an N-terminal MTS whose composition and mode of action are similar to that of *C. crescentus* BacA.

282 **BacA polymerization promotes client-protein binding**

283 The only client protein of BacA known to date is the cell wall synthase PbpC, a bitopic membrane protein
284 with a long N-terminal cytoplasmic tail, which was shown to contain the determinants mediating its bacto-
285 filin-dependent recruitment to the stalked cell pole of *C. crescentus* (Hughes et al., 2013; Kühn et al., 2010)
286 (**Figure S7A**). To clarify whether the interaction with this membrane-integral client protein contributes to
287 the association of BacA with the membrane, we compared the localization pattern of BacA-Venus in wild-
288 type and Δ*pbpC* cells. Importantly, the behavior of the fusion protein was unchanged in the mutant
289 background, suggesting that PbpC does not have a significant role in BacA polymerization or membrane
290 binding (**Figure S7B**).

291 To further clarify the interactions that promote the formation of bactofilin-client complexes at the cyto-
292 plasmic membrane, we aimed to pinpoint the parts of PbpC that mediate its recruitment to BacA. For this
293 purpose, we retrieved the amino acid sequences of PbpC homologs and aligned their predicted cytoplas-
294 mic tails (**Figure S8**). This analysis identified four distinct segments, including a highly conserved peptide

295 at the N-terminal end of PbpC (region C1), a proline-rich region, another highly conserved peptide (Region
296 C2) and a region rich in positively charged amino acids immediately adjacent to the transmembrane helix.
297 To assess the importance of these segments, we generated mVenus-tagged variants of PbpC whose
298 cytoplasmic tail either lacked region C1 (Δ2-13) or only comprised region C1, with the remaining parts
299 being replaced by an unstructured region taken from the periplasmic protein DipM of *C. crescentus*
300 (Izquierdo-Martinez et al., 2023) (**Figure S9**). Microscopic analysis showed that the removal of region C1
301 resulted in the loss of polar localization, whereas the chimeric variant showed the same localization
302 pattern as the wild-type fusion protein (**Figure 8A**). Region C1 thus appears to be necessary and sufficient
303 for the recruitment of PbpC to the cell pole-associated BacA assembly. To verify the ability of region C1 to
304 directly associate with BacA, we generated a synthetic peptide comprising the N-terminal 13 residues of
305 PbpC and analyzed its interaction with purified BacA polymers using biolayer interferometry. When
306 biosensors carrying the immobilized peptide were titrated with increasing concentrations of BacA, we
307 observed specific binding with an apparent equilibrium dissociation constant (K_D) of 4.9 µM (**Figures 8B**
308 **and S10**). A similar assay with the polymerization-deficient F130R variant, by contrast, only yielded
309 residual binding with very fast dissociation rates (**Figure 8C**). These results indicate that BacA assembly is
310 a prerequisite for efficient and stable PbpC binding, likely because the high local accumulation of BacA
311 within polymers leads to an increase in the avidity for its interaction partner.

312 Having identified a direct association of BacA with the N-terminal peptide of PbpC, we set out to map the
313 PbpC-binding site of BacA using hydrogen-deuterium-exchange (HDX) mass spectrometry, a method that
314 allows the detection of local shifts in the accessibility of backbone amide hydrogens induced by conform-
315 ational changes and/or ligand binding (Konermann et al., 2011). When analyzed alone, the HDX profile of
316 BacA showed very fast HDX in the N- and C-terminal regions flanking the bactofilin domain, which indi-
317 cates a high degree of disorder and thus corroborates the predicted domain structure of BacA (**Figure S11**).
318 Upon incubation with the PbpC peptide, several peptides in the C-terminal half of the central bactofilin
319 exhibited a small, yet significant decrease in the HDX rate (**Figure 8C**). The most prominent changes were
320 observed in a region close to the C-terminal polymerization interface (**Figure 8D**), opening the possibility
321 that inter-subunit interactions in the bactofilin polymer could potentially induce slight conformational
322 changes in BacA that promote PbpC binding. Together, these findings show that polymerization is not only
323 critical for the association of BacA with the cytoplasmic membrane but also for its interaction with the
324 client protein PbpC.

Discussion

325 Bactofilins are widespread among bacteria and mediate the spatial organization of diverse cellular pro-
326 cesses. Although the polymers they form are typically associated with the inner face of the cytoplasmic
327 membrane, the vast majority of bactofilin homologs lack transmembrane helices, suggesting the existence
328 of an alternative membrane-targeting mechanism. Consistent with this notion, the membrane-binding
329 activity of the bactofilin *Th*Bac from *T. thermophilus* has recently been localized to the unstructured N-
330 terminal tail of the protein, and a sequence alignment based on several well-characterized bactofilin hom-
331 ologs suggested the existence of a conserved N-terminal motif in this protein region (Deng et al., 2019).
332 Our work considerably extends these initial findings by determining the precise composition of the N-
333 terminal MTS, unraveling its mode of action and clarifying its conservation among bacteria. Moreover, we
334 reveal a mutual interdependence of membrane-binding and bactofilin polymerization and provide first
335 insights into mode of interaction between the bactofilin scaffold and membrane-associated client proteins.

336 Mutational analysis of *C. crescentus* BacA identified residues F2 and K4/K7 as key components of the BacA
337 MTS (**Figure 1B**) . This finding is explained by the results of our MD analysis, which show that the insertion
338 of F2 into the hydrophobic core of the lipid bilayer (**Figure 5**) is critical to ensure the proper positioning of
339 the MTS in the membrane, thereby promoting electrostatic interactions of the N-terminal NH_3^+ group with
340 the negatively charged lipid headgroups of phosphatidylglycerol. The positively charged ε-amino groups
341 of K4 and K7, by contrast, directly interact with these lipid headgroups, making the largest contribution
342 to the overall interaction energy (**Figure 6**). Notably, the N-terminal methionine residue of proteins is
343 usually removed after translation when followed by an amino acid with a short side chain (Hirel et al.,
344 1989). In the case of BacA, however, the bulky phenylalanine residue at position 2 presumably inhibits
345 this process, so that residue M1 may be a genuine, conserved part of the MTS. Although M1 interacts
346 most extensively with the lipid bilayer (**Figure 6**), its absence has only a moderate effect on the mem-
347 brane-binding activity of BacA *in vitro* (**Figure 3**). This observation supports the idea that most of its
348 interaction energy is contributed by the N-terminal NH_3^+ group, whereas the insertion of the M1 side chain
349 into the hydrophobic core of the membrane only serves to tune the positioning of the N-terminus at the
350 lipid-water interface. Consistent with the results of the MD simulations, the loss of either F2 or K4/K7
351 completely abolishes the membrane-binding activity of BacA (**Figures 2C and 3**). Moreover, it prevents
352 the assembly of BacA into distinct higher-order complexes (**Figure 1B**), suggesting a link between BacA
353 membrane association and polymerization. Indeed, a soluble BacA variant lacking the native MTS (Δ2-8)
354 regains the ability to form polymeric complexes when fused to a heterologous MTS from *E. coli* MreB

355 (**Figure 4C**), indicating that membrane binding is a prerequisite for efficient BacA polymerization. Con-
356 versely, polymerization appears to promote membrane binding, because the disruption of the BacA
357 polymerization interface (F130R) strongly increases the fraction of soluble protein (**Figure 4**). These results
358 point to a mutually cooperative binding process, whereby membrane association leads to a local increase
359 in the concentration of BacA that stimulates its self-assembly into polymers and polymerization leads to
360 a juxtaposition of MTS-containing N-terminal tails that increases the avidity of BacA for the membrane,
361 thus shifting the equilibrium to the membrane-bound state.

362 Interestingly, substitutions in the MTS that did not completely abolish BacA assembly often led to the
363 formation of multiple and/or mislocalized complexes (**Figure S2**). The mechanism determining the polar
364 localization of BacA is still unclear. However, it is conceivable that bactofilin polymers are intrinsically
365 curved and thus preferentially associate with membrane regions of positive or negative Gaussian curva-
366 ture (Kühn et al., 2010; Pöhl et al., 2024). Alternatively, the MTS may preferentially bind certain lipid
367 species that are enriched in the polar regions of the cell, with its modification leading to a change in the
368 lipid specificity that interferes with this recruitment pathway. Exchanges at less critical positions of the
369 MTS may affect these recruitment mechanisms by reducing the membrane-binding affinity and thus, in-
370 directly, also the dimensions of BacA polymers or by altering their lipid specificity.

371 To assess the conservation of mode of membrane association established for BacA, we conducted a com-
372 prehensive comparison of the N-terminal regions of all bactofilin homologs known to date. This analysis
373 revealed that amino acid sequences similar to the MTS of BacA are highly prevalent in a large number of
374 bactofilins from the phyla Pseudomonadota, Bacteroidota and Bacillota, strongly suggesting that MTS-
375 mediated membrane binding is a common theme among this group of proteins (**Figure 7**). Notably, how-
376 ever, the N-terminal motifs identified for bactofilin homologs from Spirochaetota and Thermodesulfo-
377 bacteriota are fundamentally different from those of the other phyla investigated (**Figures 7 and S6**), sug-
378 gesting a different mode of membrane binding or an adaptation of the MTS to distinct membrane com-
379 positions.

380 Notably, a small subset of bacterial bactofilin homologs contain an N-terminal transmembrane domain,
381 which mediates their stable insertion into the cytoplasmic membrane. While found in a diversity of bac-
382 terial phyla, these proteins are particularly abundant in the Pseudomonadota, especially in their gamma-
383 proteobacterial and alphaproteobacterial lineages (**Figure S5**). One of them, the bactofilin CcmA of *P. mir-*
384 *abilis*, has been previously investigated (Hay et al., 1999). It was shown to undergoes proteolytic process-
385 ing and exist in two forms, a full-length form that is an integral membrane protein and a shorter form that

386 lacks the N-terminal transmembrane segments. Intriguingly, the shorter form has an N-terminal sequence
387 (MFSRKTE) that corresponds to the predicted consensus sequence of the MTS in Pseudomonadota and,
388 indeed, behaves like a typical peripheral membrane protein. The specific functional properties conferred
389 by these two distinct modes of membrane association are still unclear. However, it is tempting to spec-
390 ulate that the assembly of MTS-containing bactofilins could be dynamically regulated by cell cycle-
391 dependent changes in membrane curvature or composition, whereas homologs with transmembrane do-
392 mains may form static polymeric assemblies. Consistent with this idea, *C. crescentus* BacA only assembles
393 at the old cell pole once its cell envelope bulges outward to initiate stalk formation, thereby establishing
394 a region of positive Gaussian curvature, although its cytoplasmic levels remain constant throughout the
395 cell cycle (Kühn et al., 2010). Similarly, the BacA homolog of the stalked budding bacterium *H. neptunium*
396 consistently assembles in regions of positive Gaussian curvature, first localizing to the stalked pole and
397 then, once the terminal segment of the stalk starts to expand into a bud, to the bud neck (Pöhl et al.,
398 2024).

399 Instead of using an MTS or a transmembrane domain, some bactofilins may also interact with the mem-
400 brane indirectly by binding to other membrane-associated proteins, as recently suggested for the bacto-
401 filin homolog CcmA from *H. pylori* (Sichel et al., 2022). It was therefore conceivable that the recruitment
402 of its client protein PbpC could contribute to the membrane-binding activity of *C. crescentus* BacA. How-
403 ever, we did not observe any obvious localization defects in a Δ*pbpC* mutant (**Figure S7A**), suggesting that
404 client binding is not critical for its proper assembly and positioning.

405 Notably, the determinants mediating the interaction of membrane-associated bactofilin scaffolds with
406 their client proteins are still poorly understood. For *M. xanthus* BacP, the binding site for its soluble inter-
407 actor PadC was shown to be located in the exceptionally long unstructured C-terminal tail, which contains
408 a conserved KKKVVVKK motif potentially involved in the interaction (Anand et al., 2020; Lin et al., 2017).
409 However, most bactofilin homologs have much shorter C-terminal tails, which are typically poorly con-
410 served in sequence and, at least in certain cases, dispensable for function *in vivo* (Sichel et al., 2022),
411 suggesting a direct interaction of client proteins with the bactofilin core domain. Our results indeed
412 suggest that the N-terminal unstructured region of PbpC associates with a C-terminal region of the bacto-
413 filin domain, close to the polymerization interface. Importantly, BacA assembly appears to be critical for
414 PbpC binding *in vitro* (**Figure 8C**), suggesting that inter-subunit contacts could potentially change the
415 conformation of BacA such as to increase its affinity for its client protein. Alternatively, polymers may
416 have a higher avidity for PbpC than BacA monomers. Polymerization thus acts as a trigger for both mem-

417 brane association and the recruitment of client proteins, ensuring the tight regulation of bactofilin
418 function.

419 Collectively, our findings provide important new insights into the function of bactofilins and the nucleo-
420 tide-independent dynamics of their assembly. It will be interesting to analyze the effect of cell cycle- or
421 stress-induced changes in membrane composition on the membrane-binding and polymerization be-
422 havior of MTS-containing bactofilin homologs. Moreover, it will be critical to investigate the mode of
423 membrane binding for bactofilins with conserved N-terminal sequences that are clearly distinct from the
424 global consensus motif.

Material and methods

425 **Media and growth conditions**

426 *C. crescentus* CB15N and its derivates were cultivated aerobically at 28 ºC in PYE rich medium (Poindexter,
427 1964) or M2G minimal medium (Ely, 1991). When required, media were supplemented with antibiotics at
428 the following concentrations (mg ml^{-1} in liquid/solid media): kanamycin (5/25 µg/ml), streptomycin (5/5
429 µg/ml) or gentamicin (0.5/5 µg/ml). *E. coli* strains are grown aerobically at 37 ºC in LB medium containing
430 antibiotics at the following concentrations (mg ml^{-1} in liquid/solid media): ampicillin (200/200), chloram-
431 phenicol (20/30), or kanamycin (30/50). To induce gene expression, media were supplemented with 0.005%
432 or 0.03% D-xylose, 0.001% L-arabinose or 1 mM IPTG when necessary.

433 **Construction of plasmids and strains**

434 The bacterial strains and plasmids used in this work are described in **Tables S2** and **S3**. The oligonucleo-
435 tides used for their construction are listed in **Table S4**. All plasmids were verified by DNA sequencing. *C.*
436 *crescentus* was transformed by electroporation (Ely, 1991). Non-replicating plasmids were integrated into
437 the chromosome by single homologous recombination at the *xylX* locus (Thanbichler et al., 2007). Proper
438 chromosomal integration was verified by colony PCR.

439 **Live-cell imaging**

440 To prepare samples for microscopy, overnight cultures were diluted to an OD_{600} of 0.1 and cultivated for
441 1 h prior to the addition of 0.005% D-xylose. After a further 1 h (BacA variants) or 2 h (PbpC variants) of
442 incubation, the cultures were diluted tenfold and samples (1.5 µl) of the suspensions were spotted on 1%
443 agarose pads prepared with $_{dd}H_2O$. Images were taken with an Axio Observer.Z1 microscope (Zeiss,
444 Germany) equipped with a Plan Apochromat 100x/1.45 Oil DIC, a Plan Apochromat 100x/1.4 Oil Ph3 M27
445 objective and a pco.edge 4.2 sCMOS camera (PCO, Germany). An X-Cite® 120PC metal halide light source
446 (EXFO, Canada) and appropriate filter cubes (ET-CFP, ET-YFP or ET-TaxasRed; Chroma, USA) were used for
447 fluorescence detection. Images were recorded with VisiView 3.3.0.6 (Visitron Systems, Germany) and
448 processed with Fiji 2.14.0/1.54f (Schindelin et al., 2012) and Adobe Illustrator CS6 (Adobe Systems, USA).
449 The subcellular distribution of fluorescence signals was analyzed with BacStalk (Hartmann et al., 2020).

450 **Single-particle tracking**

451 For single-particle tracking, cells were cultivated in M2G minimal media at 28 ºC. In the early exponential
452 growth phase, the expression of genes placed under the control of the *xylX* (P_{xyl}) promoter was induced
453 by the addition of 0.005% D-xylose. After another 3 h of incubation, cells were spotted on coverslips (25

454 mm diameter; Menzel Gläser, Germany) and covered with 1% agarose pads prepared with $_{dd}H_2O$. All
455 coverslips were cleaned before use by sonication in 2% (v/v) Hellmanex II solution (Hellma, Germany) for
456 30 min at 37 ºC, followed by rinsing in distilled water and a second round of sonication in double-distilled
457 water. Images were taken at 30-ms intervals by slimfield microscopy (Plank et al., 2009), using an Olympus
458 IX-71 microscope equipped with a UAPON 100x/ NA 1.49 TIRF objective, a back-illuminated electron-
459 multiplying charge-coupled device (EMCCD) iXon Ultra camera (Andor Solis, USA) in stream acquisition
460 mode, and a LuxX 457-100 (457 nm, 100 mW) light-emitting diode laser (Omicron-Laserage Laserprodukte
461 GmbH, Germany) as an excitation light source. The laser beam was focused onto the back focal plane and
462 operated during image acquisition with up to 2 mW (60 W cm^{-2} at the image plane). Andor Solis 4.21 soft-
463 ware was used for camera control and stream acquisition. During the first ~500 frames, most fluorescent
464 proteins in the cell were bleached to reach the single-molecule level. Subsequently, remaining and newly
465 synthesized molecules were tracked over ~2,500 frames. Prior to analysis, the frames recorded before
466 reaching the single-molecule level were removed from the streams, using the photobleaching curves as a
467 reference, and the proper pixel size (100 nm) and time increment were adjusted in the imaging metadata
468 using Fiji (Schindelin et al., 2012). Subsequently, cell meshes were determined using Oufti (Paintdakhi et
469 al., 2016) and single particles were tracked with u-track 2.2.0 (Jaqaman et al., 2008). After the removal of
470 all trajectories that were shorter than five steps, the diffusional behavior of the tracked particles was
471 analyzed using SMTracker 2.0 (Oviedo-Bocanegra et al., 2021).

472 **Cell fractionation**

473 Overnight cultures were diluted to an OD_{600} of 0.1 and grown for 2 h prior to the addition of D-xylose to a
474 final concentration of 0.03%. The cells were further cultivated for 1 h (*bacA-mVenus* alleles) or 2 h (*creS-*
475 *mNeonGreen*) to allow the expression of the genes of interest. Subsequently, cells from 5 ml culture were
476 harvested by centrifugation, washed with 0.2 M Tris-HCl (pH 8.0) and stored at -80 ºC. For further pro-
477 cessing, the pelleted cells were resuspended in a buffer containing 60 mM Tris-HCl (pH 8.0), 0.2 M sucrose,
478 0.2 M EDTA, 100 µg ml^{-1} phenylmethylsulfonyl fluoride (PMSF) and 10 µg ml^{-1} DNase I and lysed by soni-
479 cation at 30% amplitude for 7.5 min with alternating 10-s on and off phases (Model 120 Sonic Dis-
480 membrator; Fisher Scientific, USA). The lysates were centrifuged at for 10 min at 4,000 ×g (4 ºC) to remove
481 incompletely lysed cells, followed by ultracentrifugation for 1 h at 133,000 ×g (4 ºC) to separate the
482 soluble and membrane fractions. The supernatants were carefully removed, and the pellets were resus-
483 pended in an equal volume of 0.2 M Tris-HCl (pH 8.0). Both fractions were then subjected to immunoblot
484 analysis with a polyclonal anti-GFP antibody (Sigma, Germany; Cat. #: G1544; RRID: AB_439690), a

485 monoclonal anti-mNeonGreen antibody (Chromotek, Germany; Cat. #: 32f6; RRID: AB_2827566), anti-
486 MipZ antiserum (Thanbichler and Shapiro, 2006), or anti-FlgH antiserum (Mohr et al., 1996) at dilutions of
487 1:10,000, 1:1,000, 1:10,000 and 1:10,000 respectively. Goat anti-rabbit immunoglobulin G conjugated
488 with horseradish peroxidase (Perkin Elmer, USA) or goat anti-mouse immuneglobulin G conjugated with
489 horseradish peroxidase (Sigma, Germany) were used as secondary antibodies. Immunocomplexes were
490 detected with the Western Lightning Plus-ECL chemiluminescence reagent (Perkin Elmer, USA). The sig-
491 nals were recorded with a ChemiDoc MP imaging system (BioRad, Germany) and analyzed using Image
492 Lab software (BioRad, Germany).

493 **Protein purification**

494 To overproduce His_6-SUMO-BacA or mutant variants thereof, *E. coli* Rosetta(DE3)/pLysS cells transformed
495 with the appropriate plasmids were grown overnight at 37 ºC, diluted 100-fold into 3 l of LB medium
496 containing antibiotics and cultivated to an OD_{600} of ~0.6. Subsequently, the media were supplemented
497 with IPTG to a final concentration of 1 mM, and the cells were incubated for another 4 h before they were
498 harvested by centrifugation and stored at -80 ºC until further use. To purify the fusion proteins, the
499 pelleted cells were resuspended in buffer B (50 mM Tris/HCl pH 8.0, 300 mM NaCl, 0.1 mM EDTA, 5%
500 glycerol and 20 mM imidazole) supplemented with 10 µg/ml DNase I and 100 µg/ml PMSF and lysed by
501 three passages through a French press at 16,000 psi to break cells. The crude cell extract was cleared by
502 centrifugation for 30 min at 16,000 ×rpm (4 ºC) and loaded onto a 5 ml HisTrap™ HP affinity column (GE
503 Healthcare, USA) equilibrated with buffer B. After washing of the column with 50 ml of buffer B, protein
504 was eluted with a 50-ml linear gradient of imidazole (20-250 mM imidazole in buffer B). Fractions that
505 were highly enriched in the protein of interest were supplemented with 200 µg Ulp1-His_6 protease
506 (Marblestone et al., 2006) and dialyzed overnight at 4 ºC against buffer C (50 mM Tris-HCl pH 8.0, 300 mM
507 NaCl, 0.1 mM EDTA, 5% glycerol, 1 mM DTT) to cleave off the His_6-SUMO tag and remove the imidazole.
508 Subsequently, the protein solution was again applied to a 5 ml HisTrap™ HP affinity column to separate
509 the untagged BacA protein from His_6-SUMO and Ulp1-His_6. The flow-through fractions were collected and
510 analyzed by SDS-PAGE. Fractions containing the desired protein in high amount and purity were dialyzed
511 against buffer D (50 mM Tris-HCl pH 8.0, 200 mM NaCl, 0.1 mM EDTA, 5% glycerol) ($BacA_{\Delta 2\text{-}8}$) or buffer E
512 (50 mM MOPS-NaOH pH 7.0, 200 mM NaCl, 0.1 mM EDTA, 5% glycerol) (all other BacA variants). The
513 protein solutions were then concentrated using Amicon Ultra Centrifugal Filter (10 kDa MWCO) ultra-
514 filtration devices (Millipore, Germany) and stored in small aliquots at -80 °C.

515 **Preparation of liposomes**

516 Liposomes were generated from 1-palmitoyl-2-oleoyl-sn-glycero-3-phospho-(1'-rac-glycerol) (16:0-18:1
517 PG) (10 mg/mL in chloroform; Avanti Polar Lipids, USA). Chloroform was evaporated in a rotatory eva-
518 porator, resulting in a lipid film that was left to dry overnight. Subsequently, the lipids were resuspended
519 in liposome buffer (50 mM MOPS-NaOH pH 7.0, 200 mM NaCl), and the mixture was incubated at room
520 temperature for 1 h with periodic vigorous agitation. To prepare small unilamellar vesicles (SUVs) with an
521 average diameter of 100 nm, the final lipid solution (20 mg ml^{-1}) was extruded at least ten times through
522 a Mini Extruder (Avanti Polar Lipids, USA) equipped with polycarbonate membranes of 0.1 µm pore size,
523 until the solution was clear.

524 **Co-sedimentation assay**

525 Protein (20 µM) was incubated for 20 min at room temperature with or without liposomes (0.4 mg ml^{-1})
526 in binding buffer (50 mM MOPS-NaOH pH 7.0, 300 mM NaCl) in a total reaction volume of 100 µl. The
527 mixtures were then centrifuged for 20 min at 100,000 ×g (20 °C) in a TLA-55 rotor (Beckman Coulter,
528 Germany). After transfer of the supernatant to a reaction tube and resuspension of the pellet in 100 µl of
529 liposome buffer (50 mM MOPS-NaOH pH 7.0, 200 mM NaCl), samples of the two fractions were mixed
530 with SDS-PAGE sample buffer, heated at 95 °C for 10 min and loaded onto a 15% SDS-polyacrylamide gel.
531 After electrophoresis, protein was stained with Coomassie Brilliant Blue R-250. The gels were imaged in a
532 ChemiDoc MP imaging system (BioRad, Germany) using Image Lab software (BioRad, Germany), and the
533 intensity of protein bands was quantified using Fiji 2.14.0/1.54f (Schindelin et al., 2012).

534 **Bio-layer interferometry**

535 Bio-layer interferometry experiments were conducted using a BLItz system equipped with Octet® High
536 Precision Streptavidin 2.0 (SAX2) Biosensors (Satorius, Germany). In the initial step, an N-terminally bio-
537 tinylated $PbpC_{aa1-13}$ peptide (Biotin-Ahx-MNDWTLPPYKFDD; GenScript, USA) was immobilized on the
538 sensor. After the establishment of a stable baseline, association reactions were monitored with BacA at
539 various concentrations or with different BacA variants of the same concentration. At the end of each bind-
540 ing step, the sensor was transferred into an analyte-free buffer to measure the dissociation kinetics. The
541 extent of non-specific binding was assessed by monitoring the interaction of the analyte with unmodified
542 sensors. All analyses were performed in BLItz binding buffer (50 mM MOPS/NaOH pH 7.0, 100 mM NaCl,
543 1 mM EDTA, 5% glycerol, 10 µM BSA, 0.01 % Tween)

544 **Hydrogen-deuterium exchange mass spectrometry**

545 Samples were prepared using a two-arm robotic autosampler (LEAP technologies, Denmark). 7.5 µl of
546 BacA (25 µM) or a mixture of BacA (25 µM) and $PbpC_{aa1-13}$ (100 µM) were mixed with 67.5 µl of D_2O-
547 containing buffer (20 mM HEPES-NaOH pH 8.0, 300 mM NaCl) to start the exchange reaction. After 10,
548 100, 1,000 and 10,000 sec of incubation at 25 °C, 55 µl samples were taken from the reaction and mixed
549 with an equal volume of quench buffer (400 mM KH_2PO_4/H_3PO_4, 2 M guanidine-HCl, pH 2.2) kept at 1 °C.
550 95 µl of the resulting mixture were immediately injected into an ACQUITY UPLC M-class system with HDX
551 technology (Waters™, USA) (Wales et al., 2008). Undeuterated samples of BacA and a mixture of BacA
552 and $PbpC_{aa1-13}$ were prepared similarly by 10-fold dilution into H_2O-containing buffer. Proteins were di-
553 gested online on an Enzymate BEH Pepsin column (300 Å, 5 µm, 2.1 mm × 30 mm; Waters™, USA) at 12 °C
554 with a constant flow (100 µl min^{-1}) of 0.1 % (v/v) formic acid in water, and the resulting peptic peptides
555 were collected on a trap column (2 mm × 2 cm) that was filled with POROS 20 R2 material (Thermo Fisher
556 Scientific, USA) and kept at 0.5 °C. After 3 min, the trap column was placed in line with an ACQUITY UPLC
557 BEH C18 1.7 µm 1.0 × 100 mm column (Waters™, USA), and the peptides were eluted at 0.5 °C using a
558 gradient of 0.1 % (v/v) formic acid in water (A) and 0.1 % (v/v) formic acid in acetonitrile (B) at a flow rate
559 of 30 µl/min generated as follows: 0-7 min/95-65 % A, 7-8 min/65-15 % A, 8-10 min/15 % A, 10-11 min/5 %
560 A, 11-16 min/95 % A. Peptides were ionized with an electrospray ionization source operated at 250 °C
561 capillary temperature and a spray voltage of 3.0 kV. Mass spectra were acquired over a range of 50 to
562 2,000 m/z on a G2-Si HDMS mass spectrometer with ion mobility separation (Waters™, USA) in Enhanced
563 High Definition MS ($HDMS^E$) or High Definition MS (HDMS) mode for undeuterated and deuterated sam-
564 ples, respectively. A [Glu1]-Fibrinopeptide B standard (Waters™, USA) was employed for lock mass correc-
565 tion. After each run, the pepsin column was washed three times with 80 µl of 4 % (v/v) acetonitrile and
566 0.5 M guanidine hydrochloride, and blanks were performed between each sample. All measurements
567 were carried out in triplicate.

568 Peptides from the non-deuterated samples (acquired with $HDMS^E$) were identified with the ProteinLynx
569 Global SERVER (PLGS, Waters™, USA), employing low energy, elevated energy and intensity thresholds of
570 300, 100 and 1000 counts, respectively. Peptides were matched using a database containing the amino
571 acid sequences of the proteins of interest, pepsin and their reversed sequences. The search parameters
572 were as follows: peptide tolerance = automatic; fragment tolerance = automatic; min fragment ion match-
573 es per peptide = 1; min fragment ion matches per protein = 7; min peptide matches per protein = 3;
574 maximum hits to return = 20; maximum protein mass = 250,000; primary digest reagent = non-specific;
575 missed cleavages = 0; false discovery rate = 100. Deuterium incorporation was quantified with DynamX

576 3.0 (Waters™, USA), using peptides that fulfilled the following criteria: minimum intensity = 5,000 counts;
577 maximum length = 40 amino acids; minimum number of products = 2; maximum mass error = 25 ppm;
578 retention time tolerance = 0.5 min. After automated data processing with DynamX, all spectra were manu-
579 ally inspected and, if necessary, peptides were omitted (e.g. in case of a low signal-to-noise ratio or the
580 presence of overlapping peptides).

581 **Bioinformatic analysis**

582 Nucleotide and protein sequences were obtained from the National Center for Biotechnology Information
583 (NCBI) or UniProt (UniProt Consortium, 2023) databases, respectively. Sequences were compared and
584 analyzed using the blastn, blastp or PSI-blast algorithm as implemented on the NCBI website. The presence
585 of putative amphipathic helices was assessed using AMPHIPASEEK (Sapay et al., 2006). Multiple sequence
586 alignments were generated with MUSCLE v3.8.31 (Edgar, 2004) and viewed and edited with Jalview
587 (Waterhouse et al., 2009).

588 To analyze bactofilin homologues obtained from UniProt, a Python-based pre-processing procedure was
589 used, involving the exclusion of non-bacterial entries, the removal of sequences with predicted trans-
590 membrane helices and the elimination of sequences lacking detailed phylogenetic information. Addition-
591 ally, highly similar sequences (with over 90% similarity) from the same species were filtered out to correct
592 biases due to over-sequencing. The N-terminal region of each protein was determined using hmmscan
593 (HMMER 3.3.2) (Eddy, 2011) with the hidden Markov profile constructed from the seed alignment of the
594 bactofilin domain downloaded from the Pfam database (Paysan-Lafosse et al., 2022). Subsequently,
595 sequences with N-terminal regions shorter than 8 amino acids were eliminated. The resulting set of
596 sequences was categorized by phylum, and MEME (Bailey and Elkan, 1994) was used to detect the 10
597 most probable motifs. The analysis employed the following settings: classical objective function, with zero
598 or one occurrence per sequence, motif width ranging from 5 to 50 amino acids, and a 0th-order back-
599 ground Markov model.

600 **Molecular dynamics simulations**

601 All molecular dynamics (MD) simulations were carried out with Gromacs (version 2021.1) (Abraham et al.,
602 2015). The simulation systems were set up and prepared for MD simulation with the Charmm-GUI (Jo et
603 al., 2008; Jo et al., 2009; Lee et al., 2016; Wu et al., 2014),using the Charmm36m force field (Huang et al.,
604 2017) for the peptide and lipids together with the Charmm-specific TIP3P water model. The lipid composi-
605 tion of the simulated bilayer (**Table S1**) was chosen such that it mimics as closely as possible the *C. cres-*
606 *centus* membrane (Chow and Schmidt, 1974; De Siervo and Homola, 1980). Symmetric bilayers with 128

607 lipids in each monolayer were constructed, that is, the same number and type of lipids was present in the
608 two leaflets. At the beginning of the simulations, a single bactofilin 10mer peptide (either the wild-type
609 sequence MFSKQAKSNN, or the K4SK7S or F2Y mutants) were modeled as extended conformations and
610 placed in the bulk water phase, located at least 3 nm away from the lipid headgroups. The net charge of
611 the simulation box was neutralized with 150 mM KCl. After energy minimization (with steepest descent),
612 MD simulations were carried out with periodic boundary conditions in the NpT ensemble at a constant
613 temperature of 310 K, maintained via the Bussi velocity-rescaling thermostat (Bussi et al., 2007), and con-
614 stant 1 bar pressure, maintained by semi-isotropic pressure coupling of the lateral (x,y) and normal (z)
615 dimensions of the simulation box to a weak coupling barostat(Berendsen et al., 1984). Short-range
616 Coulomb and Lennard-Jones 6,12 interactions were described with a buffered pair list (Páll and Hess, 2013)
617 with potentials smoothly shifted to zero at a 1.2 nm distance, with forces switched to zero between 1.0
618 and 1.2 nm. The long-range electrostatic interactions were described with the particle mesh Ewald (PME)
619 method with 0.12 nm grid spacing (Darden et al., 1993). The LINCS and SETTLE algorithms were used to
620 constrain all protein bonds involving H-atoms and to keep the water molecules rigid, respectively, allowing
621 to integrate the equations of motion with 2 fs time steps using the leap-frog integrator. The final produc-
622 tion MD simulations were 500 ns long.

623 **Data analysis**

624 Data were analyzed in Excel 2019 (Microsoft) or Python 3.10.12 and mainly visualized using the Python
625 Matplotlib v3.6.2 (Hunter, 2007) and Seaborn v0.12.2 (Waskom, 2021) libraries. The plots obtained were
626 edited with Adobe Illustrator CS6 (Adobe Systems) to generate the final figures.

627 **Statistics and reproducibility**

628 All experiments were performed at least twice independently with similar results. No data were excluded
629 from the analyses. To quantify imaging data, multiple images were analyzed per condition. The analyses
630 included all cells in the images or, in the case of high cell densities, all cells in a square portion of the
631 images. The selection of the images and fields of cells analyzed was performed randomly.

632 **Availability of biological material**

633 The plasmids and strains used in this study are available from the corresponding author upon request.

634 **Data availability**

635 All data generated in this study are included in the manuscript and the supplementary material.

Acknowledgements

We thank Julia Rosum for excellent technical assistance and Rogelio Hernandez-Tamayo for initial support with the single-particle tracking analysis. This work was supported by the University of Marburg (core funding to M.T.), the Max Planck Society (Max Planck Fellowship to M.T.), the German Research Foundation (project 450420164 – TH 885/3-1 to M.T. and EXC 2033 – 390677874 – RESOLV to L.V.S.), and the European Union's Horizon 2020 research and innovation programme (Marie Sklodowska-Curie grant agreement No 801459 – FP-RESOMUS).

Author contributions

Y.L. and M.T. conceived the study. Y.L. performed the cell biological, biochemical and bioinformatic analyses. R.K. conducted the MD simulations and analyzed them together with S.M. and L.V.S. W.S. performed the HDX mass spectrometry analysis. Y.L., W.S. and M.T. analyzed the experimental data. G.B., L.V.S. and M.T. secured funding and supervised the study. Y.L. and M.T. wrote the paper, with input from all other authors.

Competing interests

The author declare no competing interests.

Figure legends

648 **Figure 1. Identification of residues critical for the membrane-binding activity of BacA *in vivo*. (A)** Sche-
649 matic representation of the BacA-mVenus fusion protein used in this study. The proposed membrane-
650 targeting sequence is highlighted in red. The sequence at the botton shows that result of an amphipathic
651 helix prediction for BacA using the AMPHIPASEEK software (Sapay et al., 2006). Residues predicted to be
652 located in an unstructured, randomly coiled region are labeled with "c". **(B)** Localization patterns of
653 mutant BacA-mVenus variants. Δ*bacAB* cells producing BacA-mVenus or mutant variants thereof (LY84,
654 LY89, LY90, LY97, LY111, LY112, LY113, LY119) were analyzed by phase contrast and fluorescence micros-
655 copy. The outlines of the cells are shown in the fluorescence images. Demographs summarizing the single-
656 cell fluorescence profiles obtained from random subpopulations of cells are given next to the respective
657 fluorescence images. The numbers of cells analyzed are: WT (130), Δ2-8 (292), F130R (156), F2Y (138), F2E
658 (194), K4S-K7S (151), K4E-K7E (382), F2E-K4E-K7E (130). The vertical red line indicates the junction bet-
659 ween cell body and the stalk. Scale bar: 1 µm. **(C)** Helical wheel diagram of the first eight amino acids of
660 BacA. Residues are colored by properties: hydrophobic (gray), basic (blue), uncharged (yellow).

661 **Figure 2. Verification of residues M1, F2 and K4/K7 as critical components of the BacA MTS. (A)** Mobility
662 of the indicated BacA-mVenus fusion proteins. Shown is the average mean-squared displacement (MSD)
663 (± SD) as a function of time, based on single-particle tracking analysis. **(B)** Cell fractionation experiment
664 investigating the membrane-binding activity of BacA-mVenus (WT) or a mutant variant lacking the
665 predicted MTS (Δ2-8). Whole-cell lysates (W) as well as the soluble (S) and pellet (P) fractions of cells
666 producing the indicated proteins were subjected to immunoblot analysis with an anti-GFP antibody,
667 detecting the BacA-mVenus fusion protein. As controls, the same samples were probed with antibodies
668 raised against the soluble cell division regulator MipZ (Thanbichler and Shapiro, 2006) or the membrane-
669 bound flagellar L-ring subunit FlgH (Mohr et al., 1996) from *C. crescentus*. **(C)** As in panel C, but for cells
670 producing mutant BacA-mVenus variants with single or multiple amino-acid exchanges in the predicted
671 MTS. Shown are representative images (n=3 independent replicates). The strains used are given in the
672 legend to Figure 1B.

673 **Figure 3. Co-sedimentation analysis of the association of various BacA variants with liposomes.** The
674 indicated proteins (20 µM) were incubated without (-) or with (+) liposomes (0.4 mg/mL) prior to ultra-
675 centrifugation. The supernatant (S) and pellet (P) fractions of each mixture were analyzed by SDS gel elec-
676 trophoresis. Shown are scans of representative gels and a quantification of the average amount of protein
677 (± SD) contained in the different fractions (n=3 independent replicates).

678 **Figure 4. Interdependence of BacA polymerization and membrane binding. (A)** Cell fractionation experi-
679 ment investigating the membrane-binding activity of the polymerization-deficient F130R variant of BacA-
680 mVenus *in vivo* (LY119). The analysis was performed as described for **Figure 2B**. **(B)** Co-sedimentation
681 analysis of the association of BacA-F130R with liposomes *in vitro*, performed as described for **Figure 3**. **(C)**
682 Role of polymerization in the membrane association of a BacA-mVenus variant carrying the membrane-
683 targeting sequence of *E. coli* MreB. Shown are phase contrast and fluorescence images of Δ*bacAB* mutants
684 (LY103, LY123) producing either a BacA-mVenus variant in which the MTS is replaced by two tandem
685 copies of the N-terminal amphiphilic helix of *E. coli* MreB (^{MreB}WT) or a polymerization-deficient variant
686 thereof (^{MreB}F130A). Demographs summarizing the single-cell fluorescence profiles obtained from random
687 subpopulations of cells are given next to the respective fluorescence images. The numbers of cells anal-
688 yzed are: ^{MreB}WT (126), ^{MreB}F130A (169). The vertical red line indicates the junction between cell body and
689 the stalk. Scale bar: 1 µm. **(D)** Mobility of the indicated BacA-mVenus fusion proteins. Shown is the average
690 mean-squared displacement (MSD) (± SD) as a function of time, based on single-particle tracking analysis.
691 **(E)** Cell fractionation experiment investigating the membrane-binding activity of ^{MreB}BacA-mVenus (^{MreB}WT)
692 and its polymerization-deficient F130R variant (^{MreB}F130R) *in vivo* (LY103, LY123). The analysis was per-
693 formed as described for **Figure 2B.**

694 **Figure 5. Molecular dynamics simulation of the interaction between the BacA MTS and a model mem-**
695 **brane. (A)** Snapshot of the molecular dynamics (MD) simulation system showing the 10-mer peptide
696 MFSKQAKSNN ($BacA_{1-10}$; red) after binding to the lipid bilayer. The water is shown in surface representa-
697 tion. K^+ and Cl^- counterions are not shown. **(B)** Close-up view of a representative snapshot from the MD
698 simulation visualizing the binding mode of the peptide on the membrane surface. **(C)** Structural overlay
699 of 40 snapshots from the MD simulation, taken after constant time intervals from the trajectory. **(D)**
700 Density profiles of individual residues in the wild-type peptide along the membrane normal, i.e. the z-
701 component of the distance vector from the center-of-mass (COM) of the bilayer, with the membrane
702 midplane located at zero. The vertical dashed black line indicates the maximum of the density distribution
703 of the lipid headgroup phosphates.

704 **Figure 6. Contact numbers and interaction energies for different peptide-lipid bilayer interactions. (A)**
705 The graph shows the total number of contacts between individual residues in the wild-type, K4S-K7S and
706 F2Y peptides and the lipid bilayer as well as the number of contacts with PG lipids and GLY lipids. A contact
707 between a peptide residue and a lipid was defined to exist if any two non-hydrogen atoms of the residue
708 and a lipid molecule were within a distance of 0.5 nm to each other. Contacts were counted for each

709 frame of the MD trajectories and averaged. Multiple contacts between a peptide and a lipid molecule
710 were treated as a single contact, so that the number of contacts counted was either 1 or 0. The statistical
711 errors plotted were obtained from the difference between the two different sets of 500-ns simulations,
712 starting with peptides in an unfolded or α-helical conformation, respectively. **(B)** Energies of the inter-
713 actions between individual residues in the wild-type, K4S-K7S and F2Y peptides and the lipid bilayer. The
714 interaction energies plotted are the combined interaction energies of all Coulomb and van-der-Waals
715 interactions in the force field averaged over the simulation trajectories.

716 **Figure 7. Conservation of the N-terminal regions of bactofilin homologs in different bacterial phyla.** The
717 pie chart in the middle shows the relative distribution of the 14337 unique bactofilin homologs analyzed
718 among the indicated bacterial phyla. The sequence logos give the the most widespread N-terminal motifs
719 obtained either by a global analysis of all 14337 bactofilin sequences (global consensus) or by an analysis
720 of subsets of these sequences from specific phyla.

721 **Figure 8. Interaction of BacA with its client protein PbpC. (A)** Localization patterns of different PbpC
722 variants. Δ*bacB* Δ*pbpC* cells producing mVenus-PbpC (LY75) or mutant variants thereof lacking region C1
723 (LY76) or carrying an unstructured region from *C. crescentus* DipM in place of the unstructured region
724 connecting region C1 and the transmembrane helix (LY77) were analyzed by phase contrast and fluores-
725 cence microscopy. The outlines of the cells are shown in the fluorescence images. Demographs summariz-
726 ing the single-cell fluorescence profiles obtained from random subpopulations of cells are given next to
727 the respective fluorescence images. The numbers of cells analyzed are: LY75 (158), LY76 (253), LY77 (119).
728 Scale bar: 1 µm. **(B)** Biolayer interferometric analysis of the interaction between $PbpC_{1\text{-}13aa}$ and BacA. A
729 synthetic peptide comprising the first 13 amino acids of PbpC ($PbpC_{aa1\text{-}13}$) was immobilized on a biosensor
730 and probed with increasing concentrations of BacA. After the association step, the sensor was transferred
731 to a protein-free buffer to monitor the dissociation reaction. The graph shows a representative titration
732 series (n=3 independent replicates). **(C)** Comparison of the interaction of $PbpC_{aa1\text{-}13}$ with BacA and its
733 polymerization deficient F130R variant, performed as described in panel B. **(D)** Mapping of the PbpC
734 binding site on BacA by hydrogen-deuterium exchange (HDX) mass spectrometry. The plots show the
735 extent of deuterium uptake by three representative peptides obtained after tryptic digestion of BacA
736 protein (2.5 µM) that had been incubated in the absence or presence of $PbpC_{aa1\text{-}13}$ peptide (10 µM) for the
737 indicated time periods (see **Data S1** for the full set of peptides). **(E)** Mapping of the the differences in
738 deuterium uptake observed at t=1000 s onto the solid-state NMR structure of BacA (Shi et al., 2015).

739 # References

740 Abraham, MJ, Murtola, T, Schulz, R, Páll, S, Smith, JC, Hess, B, Lindahl, E (2015). GROMACS: High
741 performance molecular simulations through multi-level parallelism from laptops to supercomputers.
742 *SoftwareX* **1-2**:19-25.

743 Anand, D, Schumacher, D, Søgaard-Andersen, L (2020). SMC and the bactofilin/PadC scaffold have distinct
744 yet redundant functions in chromosome segregation and organization in *Myxococcus xanthus*. *Mol*
745 *Microbiol* **114**:839-856.

746 Ausmees, N, Kuhn, JR, Jacobs-Wagner, C (2003). The bacterial cytoskeleton: an intermediate filament-like
747 function in cell shape. *Cell* **115**:705-713.

748 Bailey, TL, Elkan, C (1994). Fitting a mixture model by expectation maximization to discover motifs in
749 biopolymers. *Proc Int Conf Intell Syst Mol Biol* **2**:28-36.

750 Berendsen, HJC, Postma, JPM, van Gunsteren, WF, DiNola, A, Haak, JR (1984). Molecular dynamics with
751 coupling to an external bath. *J Chem Phys* **81**:3684–3690.

752 Billini, M, Biboy, J, Kuhn, J, Vollmer, W, Thanbichler, M (2019). A specialized MreB-dependent cell wall
753 biosynthetic complex mediates the formation of stalk-specific peptidoglycan in *Caulobacter crescentus*.
754 *PLoS Genet* **15**:e1007897.

755 Brockett, MR, Lee, J, Cox, JV, Liechti, GW, Ouellette, SP (2021). A dynamic, ring-forming bactofilin critical
756 for maintaining cell size in the obligate intracellular bacterium *Chlamydia trachomatis*. *Infect Immun*
757 **89**:e0020321.

758 Bussi, G, Donadio, D, Parrinello, M (2007). Canonical sampling through velocity rescaling. *J Chem Phys*
759 **126**:014101.

760 Cabeen, MT, Jacobs-Wagner, C (2010). The bacterial cytoskeleton. *Annu Rev Genet* **44**:365-392.

761 Caccamo, PD, Jacq, M, VanNieuwenhze, MS, Brun, YV (2020). A division of labor in the recruitment and
762 topological organization of a bacterial morphogenic complex. *Curr Biol* **30**:3908-3922.

763 Chow, TC, Schmidt, JM (1974). Fatty acid composition of *Caulobacter crescentus*. *J Gen Microbiol* **83**:369-
764 373.

765 UniProt Consortium (2023). UniProt: the Universal Protein Knowledgebase in 2023. *Nucleic Acids Res*
766 **51**:D523-D531.

767 Contreras, I, Shapiro, L, Henry, S (1978). Membrane phospholipid composition of *Caulobacter crescentus*.
768 *J Bacteriol* **135**:1130-1136.

769 Darden, T, York, D, Pedersen, L (1993). Particle mesh Ewald: An N·log(N) method for Ewald sums in large
770 systems. *J Chem Phys* **98**:10089–10092.

771 De Siervo, AJ, Homola, AD (1980). Analysis of *Caulobacter crescentus* lipids. *J Bacteriol* **143**:1215-1222.

772 Deng, X, Gonzalez Llamazares, A, Wagstaff, JM, Hale, VL, Cannone, G, McLaughlin, SH, Kureisaite-Ciziene,
773 D, Löwe, J (2019). The structure of bactofilin filaments reveals their mode of membrane binding and lack
774 of polarity. *Nat Microbiol* **4**:2357-2368.

775 Eddy, SR (2011). Accelerated profile HMM searches. *PLoS Comput Biol* **7**:e1002195.

776 Edgar, RC (2004). MUSCLE: multiple sequence alignment with high accuracy and high throughput. *Nucleic*
777 *Acids Res* **32**:1792-1797.

El Andari, J, Altegoer, F, Bange, G, Graumann, PL (2015). *Bacillus subtilis* bactofilins are essential for flagellar hook- and filament assembly and dynamically localize into structures of less than 100 nm diameter underneath the cell membrane. *PLoS One* **10**:e0141546.

Ely, B (1991). Genetics of *Caulobacter crescentus*. *Methods Enzymol* **204**:372-384.

Frirdich, E, Vermeulen, J, Biboy, J, Vollmer, W, Gaynor, EC (2023). Multiple *Campylobacter jejuni* proteins affecting the peptidoglycan structure and the degree of helical cell curvature. *Front Microbiol* **14**:1162806.

Hartmann, R, van Teeseling, MCF, Thanbichler, M, Drescher, K (2020). BacStalk: A comprehensive and interactive image analysis software tool for bacterial cell biology. *Mol Microbiol* **114**:140-150.

Hay, NA, Tipper, DJ, Gygi, D, Hughes, C (1999). A novel membrane protein influencing cell shape and multicellular swarming of *Proteus mirabilis*. *J Bacteriol* **181**:2008-2016.

Hirel, PH, Schmitter, MJ, Dessen, P, Fayat, G, Blanquet, S (1989). Extent of N-terminal methionine excision from *Escherichia coli* proteins is governed by the side-chain length of the penultimate amino acid. *Proc Natl Acad Sci U S A* **86**:8247-8251.

Holtrup, S, Heimerl, T, Linne, U, Altegoer, F, Noll, F, Waidner, B (2019). Biochemical characterization of the *Helicobacter pylori* bactofilin-homolog HP1542. *PLoS One* **14**:e0218474.

Huang, J, Rauscher, S, Nawrocki, G, Ran, T, Feig, M, de Groot, BL, Grubmuller, H, MacKerell, AD, Jr. (2017). CHARMM36m: an improved force field for folded and intrinsically disordered proteins. *Nat Methods* **14**:71-73.

Hughes, HV, Lisher, JP, Hardy, GG, Kysela, DT, Arnold, RJ, Giedroc, DP, Brun, YV (2013). Co-ordinate synthesis and protein localization in a bacterial organelle by the action of a penicillin-binding-protein. *Mol Microbiol* **90**:1162-1177.

Hunter, JD (2007). Matplotlib: a 2D graphics environment. *Comput Sci Eng* **9**:90-95.

Izquierdo-Martinez, A, Billini, M, Miguel-Ruano, V, Hernandez-Tamayo, R, Richter, P, Biboy, J, Batuecas, MT, Glatter, T, Vollmer, W, Graumann, PL*, et al.* (2023). DipM controls multiple autolysins and mediates a regulatory feedback loop promoting cell constriction in *Caulobacter crescentus*. *Nat Commun* **14**:4095.

Jackson, KM, Schwartz, C, Wachter, J, Rosa, PA, Stewart, PE (2018). A widely conserved bacterial cytoskeletal component influences unique helical shape and motility of the spirochete *Leptospira biflexa*. *Mol Microbiol* **108**:77-89.

Jaqaman, K, Loerke, D, Mettlen, M, Kuwata, H, Grinstein, S, Schmid, SL, Danuser, G (2008). Robust single-particle tracking in live-cell time-lapse sequences. *Nat Methods* **5**:695-702.

Jo, S, Kim, T, Iyer, VG, Im, W (2008). CHARMM-GUI: a web-based graphical user interface for CHARMM. *J Comput Chem* **29**:1859-1865.

Jo, S, Lim, JB, Klauda, JB, Im, W (2009). CHARMM-GUI Membrane Builder for mixed bilayers and its application to yeast membranes. *Biophys J* **97**:50-58.

Jones, LJ, Carballido-Lopez, R, Errington, J (2001). Control of cell shape in bacteria: helical, actin-like filaments in *Bacillus subtilis*. *Cell* **104**:913-922.

Kassem, MM, Wang, Y, Boomsma, W, Lindorff-Larsen, K (2016). Structure of the bacterial cytoskeleton protein bactofilin by NMR chemical shifts and sequence variation. *Biophys J* **110**:2342-2348.

Koch, MK, McHugh, CA, Hoiczyk, E (2011). BacM, an N-terminally processed bactofilin of *Myxococcus xanthus*, is crucial for proper cell shape. *Mol Microbiol* **80**:1031-1051.

818 Konermann, L, Pan, J, Liu, YH (2011). Hydrogen exchange mass spectrometry for studying protein structure
819 and dynamics. *Chem Soc Rev* **40**:1224-1234.

820 Kühn, J, Briegel, A, Mörschel, E, Kahnt, J, Leser, K, Wick, S, Jensen, GJ, Thanbichler, M (2010). Bactofilins,
821 a ubiquitous class of cytoskeletal proteins mediating polar localization of a cell wall synthase in
822 *Caulobacter crescentus*. *EMBO J* **29**:327-339.

823 Lee, J, Cheng, X, Swails, JM, Yeom, MS, Eastman, PK, Lemkul, JA, Wei, S, Buckner, J, Jeong, JC, Qi, Y*, et al.*
824 (2016). CHARMM-GUI input generator for NAMD, GROMACS, AMBER, OpenMM, and CHARMM/OpenMM
825 simulations using the CHARMM36 additive force field. *J Chem Theory Comput* **12**:405-413.

826 Lee, J, Cox, JV, Ouellette, SP (2023). The unique N-terminal domain of chlamydial bactofilin mediates its
827 membrane localization and ring-forming properties. *J Bacteriol* **205**:e0009223.

828 Lin, L, Osorio Valeriano, M, Harms, A, Søgaard-Andersen, L, Thanbichler, M (2017). Bactofilin-mediated
829 organization of the ParAB*S* chromosome segregation system in *Myxococcus xanthus*. *Nat Commun* **8**:1817.

830 Liu, Y, van den Ent, F, Löwe, J (2024). Filament structure and subcellular organization of the bacterial
831 intermediate filament-like protein crescentin. *Proc Natl Acad Sci U S A* **121**:e2309984121.

832 Löwe, J, Amos, LA (1998). Crystal structure of the bacterial cell-division protein FtsZ. *Nature* **391**:203-206.

833 Marblestone, JG, Edavettal, SC, Lim, Y, Lim, P, Zuo, X, Butt, TR (2006). Comparison of SUMO fusion
834 technology with traditional gene fusion systems: enhanced expression and solubility with SUMO. *Protein*
835 *Sci* **15**:182-189.

836 McQuillen, R, Xiao, J (2020). Insights into the structure, function, and dynamics of the bacterial cytokinetic
837 FtsZ-ring. *Annu Rev Biophys* **49**:309-341.

838 Mohr, CD, Jenal, U, Shapiro, L (1996). Flagellar assembly in *Caulobacter crescentus*: a basal body P-ring
839 null mutation affects stability of the L-ring protein. *J Bacteriol* **178**:675-682.

840 Mukherjee, A, Dai, K, Lutkenhaus, J (1993). *Escherichia coli* cell division protein FtsZ is a guanine nucleotide
841 binding protein. *Proc Natl Acad Sci U S A* **90**:1053-1057.

842 Oviedo-Bocanegra, LM, Hinrichs, R, Rotter, DAO, Dersch, S, Graumann, PL (2021). Single molecule/particle
843 tracking analysis program SMTracker 2.0 reveals different dynamics of proteins within the RNA degrado-
844 some complex in *Bacillus subtilis*. *Nucleic Acids Res* **49**:e112.

845 Páll, S, Hess, B (2013). A flexible algorithm for calculating pair interactions on SIMD architectures. *Comput*
846 *Phys Commun* **184**:2641-2650.

847 Paysan-Lafosse, T, Blum, M, Chuguransky, S, Grego, T, Pinto, BL, Salazar, GA, Bileschi, ML, Bork, P, Bridge,
848 A, Colwell, L*, et al.* (2022). InterPro in 2022. *Nucleic Acids Res* **51**:D418-D427.

849 Pichoff, S, Lutkenhaus, J (2005). Tethering the Z ring to the membrane through a conserved membrane
850 targeting sequence in FtsA. *Mol Microbiol* **55**:1722-1734.

851 Plank, M, Wadhams, GH, Leake, MC (2009). Millisecond timescale slimfield imaging and automated
852 quantification of single fluorescent protein molecules for use in probing complex biological processes.
853 *Integr Biol (Camb)* **1**:602-612.

854 Pöhl, S, Osorio-Valeriano, M, Cserti, E, Harberding, J, Hernandez-Tamayo, R, Biboy, J, Sobetzko, P, Vollmer,
855 W, Graumann, PL, Thanbichler, M (2024). A dynamic bactofilin cytoskeleton cooperates with an M23
856 endopeptidase to control bacterial morphogenesis. *Elife* **12**:RP86577.

857 Poindexter, JS (1964). Biological properties and classification of the *Caulobacter* group. *Bacteriol Rev*
858 **28**:231-295.

859 Richter, P, Melzer, B, Müller, FD (2023). Interacting bactofilins impact cell shape of the MreB-less
860 multicellular *Rhodomicrobium vannielii*. *PLoS Genet* **19**:e1010788.

861 Rohs, PDA, Bernhardt, TG (2021). Growth and Division of the peptidoglycan matrix. *Annu Rev Microbiol*
862 **75**:315-336.

863 Salje, J, van den Ent, F, de Boer, P, Löwe, J (2011). Direct membrane binding by bacterial actin MreB. *Mol*
864 *Cell* **43**:478-487.

865 Sapay, N, Guermeur, Y, Deleage, G (2006). Prediction of amphipathic in-plane membrane anchors in
866 monotopic proteins using a SVM classifier. *BMC Bioinformatics* **7**:255.

867 Schindelin, J, Arganda-Carreras, I, Frise, E, Kaynig, V, Longair, M, Pietzsch, T, Preibisch, S, Rueden, C,
868 Saalfeld, S, Schmid, B*, et al.* (2012). Fiji: an open-source platform for biological-image analysis. *Nat*
869 *Methods* **9**:676-682.

870 Shi, C, Fricke, P, Lin, L, Chevelkov, V, Wegstroth, M, Giller, K, Becker, S, Thanbichler, M, Lange, A (2015).
871 Atomic-resolution structure of cytoskeletal bactofilin by solid-state NMR. *Sci Adv* **1**:e1501087.

872 Sichel, SR, Bratton, BP, Salama, NR (2022). Distinct regions of *H. pylori*'s bactofilin CcmA regulate protein-
873 protein interactions to control helical cell shape. *Elife* **11**:e80111.

874 Stankeviciute, G, Guan, Z, Goldfine, H, Klein, EA (2019). *Caulobacter crescentus* adapts to phosphate
875 starvation by synthesizing anionic glycoglycerolipids and a novel glycosphingolipid. *mBio* **10**:e00107-
876 00119.

877 Sycuro, LK, Pincus, Z, Gutierrez, KD, Biboy, J, Stern, CA, Vollmer, W, Salama, NR (2010). Peptidoglycan
878 crosslinking relaxation promotes *Helicobacter pylori*'s helical shape and stomach colonization. *Cell*
879 **141**:822-833.

880 Thanbichler, M, Iniesta, AA, Shapiro, L (2007). A comprehensive set of plasmids for vanillate- and xylose-
881 inducible gene expression in *Caulobacter crescentus*. *Nucleic Acids Res* **35**:e137.

882 Thanbichler, M, Shapiro, L (2006). MipZ, a spatial regulator coordinating chromosome segregation with
883 cell division in *Caulobacter*. *Cell* **126**:147-162.

884 van den Ent, F, Amos, LA, Löwe, J (2001). Prokaryotic origin of the actin cytoskeleton. *Nature* **413**:39-44.

885 Vasa, S, Lin, L, Shi, C, Habenstein, B, Riedel, D, Kühn, J, Thanbichler, M, Lange, A (2015). β-Helical
886 architecture of cytoskeletal bactofilin filaments revealed by solid-state NMR. *Proc Natl Acad Sci U S A*
887 **112**:E127-136.

888 Wagstaff, J, Löwe, J (2018). Prokaryotic cytoskeletons: protein filaments organizing small cells. *Nat Rev*
889 *Microbiol* **16**:187-201.

890 Wales, TE, Fadgen, KE, Gerhardt, GC, Engen, JR (2008). High-speed and high-resolution UPLC separation
891 at zero degrees Celsius. *Anal Chem* **80**:6815-6820.

892 Waskom, ML (2021). seaborn: statistical data visualization. *J Open Source Softw* **6**:3021.

893 Waterhouse, AM, Procter, JB, Martin, DM, Clamp, M, Barton, GJ (2009). Jalview Version 2 – a multiple
894 sequence alignment editor and analysis workbench. *Bioinformatics* **25**:1189-1191.

895 Wolfenden, R, Andersson, L, Cullis, PM, Southgate, CC (1981). Affinities of amino acid side chains for
896 solvent water. *Biochemistry* **20**:849-855.

897 Wu, EL, Cheng, X, Jo, S, Rui, H, Song, KC, Davila-Contreras, EM, Qi, Y, Lee, J, Monje-Galvan, V, Venable, RM*,*
898 *et al.* (2014). CHARMM-GUI Membrane Builder toward realistic biological membrane simulations. *J*
899 *Comput Chem* **35**:1997-2004.

900 Zuckerman, DM, Boucher, LE, Xie, K, Engelhardt, H, Bosch, J, Hoiczyk, E (2015). The bactofilin cytoskeleton
901 protein BacM of *Myxococcus xanthus* forms an extended β-sheet structure likely mediated by
902 hydrophobic interactions. *PLoS One* **10**:e0121074.

Figures

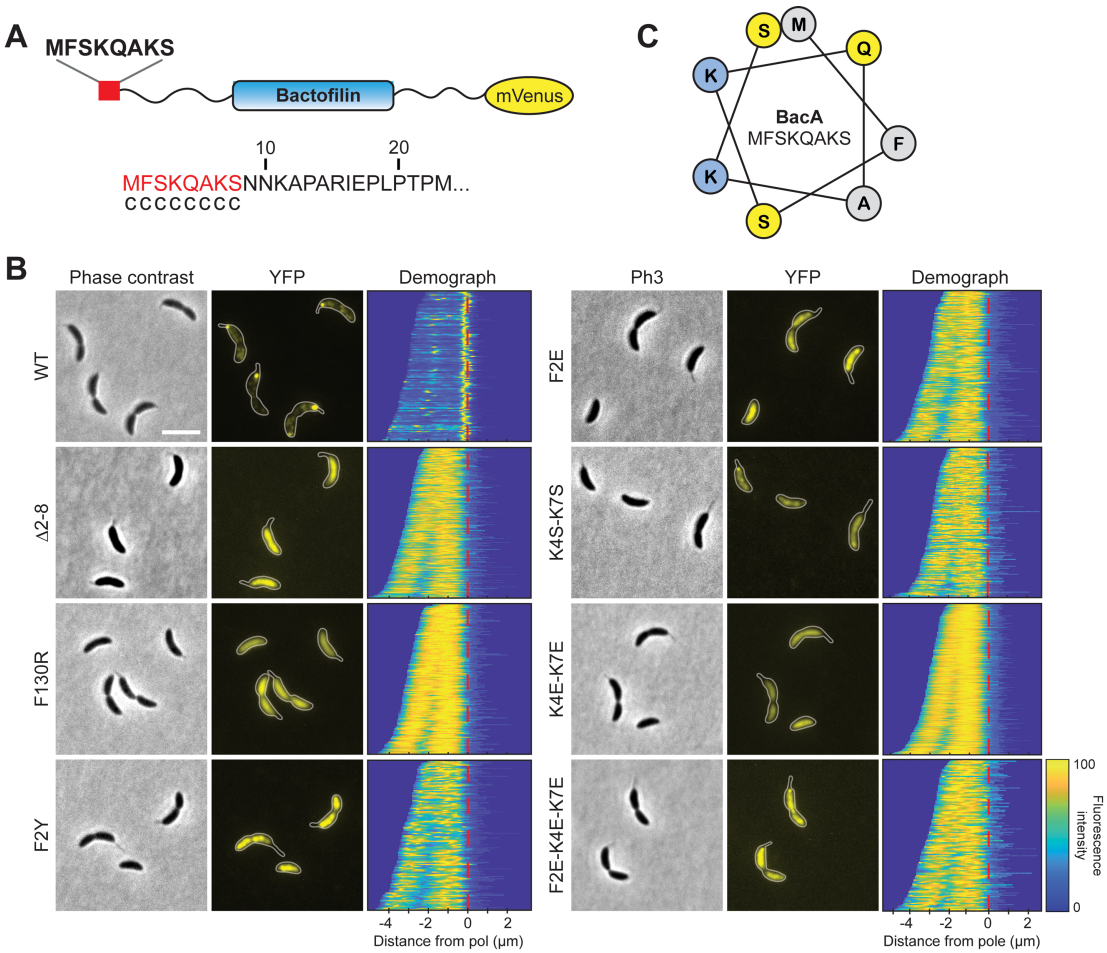

Figure 3. Identification of residues critical for the membrane-binding activity of BacA *in vivo*. (A) Schematic representation of the BacA-mVenus fusion protein used in this study. The proposed membrane-targeting sequence is highlighted in red. The sequence at the botton shows that result of an amphipathic helix prediction for BacA using the AMPHIPASEEK software (Sapay et al., 2006). Residues predicted to be located in an unstructured, randomly coiled region are labeled with "c". **(B)** Localization patterns of mutant BacA-mVenus variants. Δ*bacAB* cells producing BacA-mVenus or mutant variants thereof (LY84, LY89, LY90, LY97, LY111, LY112, LY113, LY119) were analyzed by phase contrast and fluorescence microscopy. The outlines of the cells are shown in the fluorescence images. Demographs summarizing the single-cell fluorescence profiles obtained from random sub-populations of cells are given next to the respective fluorescence images. The numbers of cells analyzed are: WT (130), Δ2-8 (292), F130R (156), F2Y (138), F2E (194), K4S-K7S (151), K4E-K7E (382), F2E-K4E-K7E (130). The vertical red line indicates the junction between cell body and the stalk. Scale bar: 1 µm. **(C)** Helical wheel diagram of the first eight amino acids of BacA. Residues are colored by properties: hydrophobic (gray), basic (blue), uncharged (yellow).

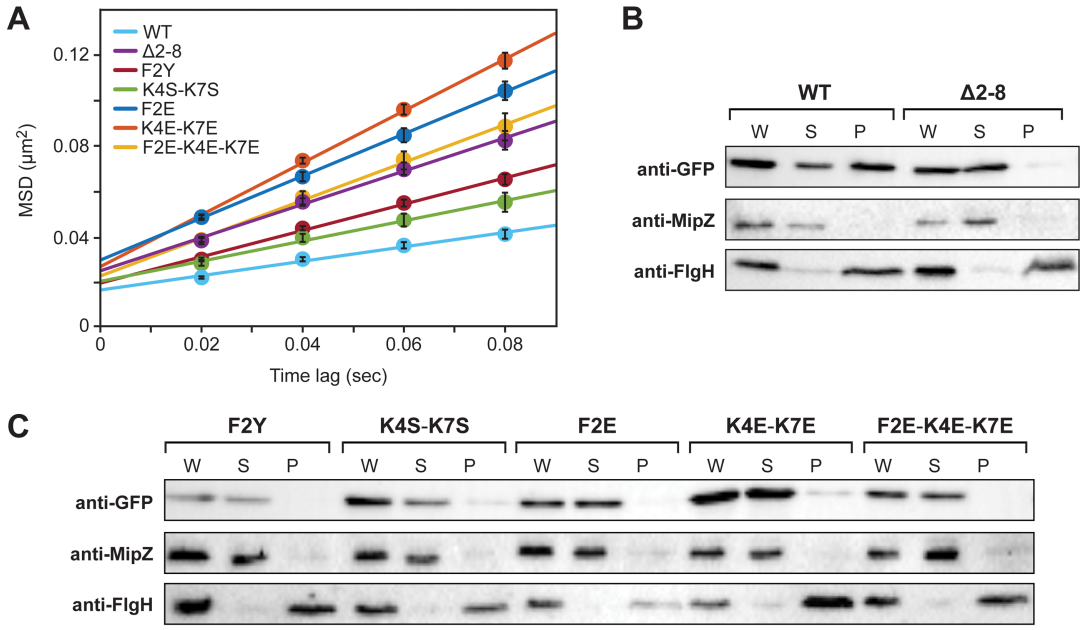

Figure 4. Verification of residues M1, F2 and K4/K7 as critical components of the BacA MTS. (A) Mobility of the indicated BacA-mVenus fusion proteins. Shown is the average mean-squared displacement (MSD) (± SD) as a function of time, based on single-particle tracking analysis. **(B)** Cell fractionation experiment investigating the membrane-binding activity of BacA-mVenus (WT) or a mutant variant lacking the predicted MTS (Δ2-8). Whole-cell lysates (W) as well as the soluble (S) and pellet (P) fractions of cells producing the indicated proteins were subjected to immunoblot analysis with an anti-GFP antibody, detecting the BacA-mVenus fusion protein. As controls, the same samples were probed with antibodies raised against the soluble cell division regulator MipZ (Thanbichler and Shapiro, 2006) or the membrane-bound flagellar L-ring subunit FlgH (Mohr et al., 1996) from *C. crescentus*. **(C)** As in panel C, but for cells producing mutant BacA-mVenus variants with single or multiple amino-acid exchanges in the predicted MTS. Shown are representative images (n=3 independent replicates). The strains used are given in the legend to Figure 1B.

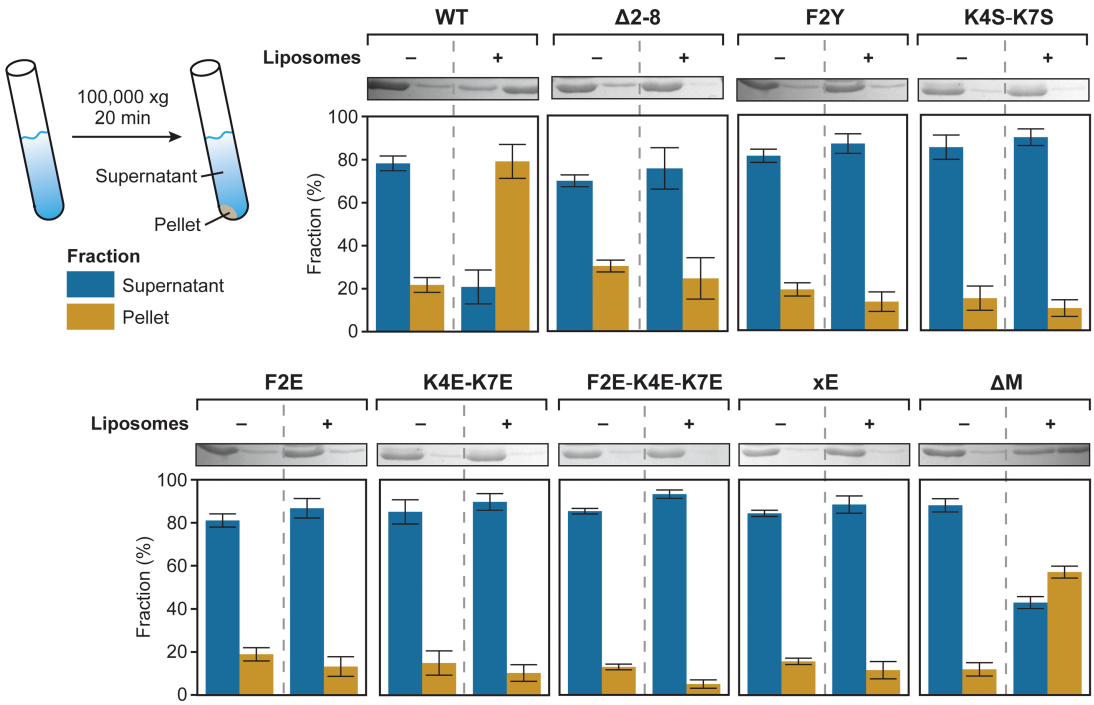

924 **Figure 3. Co-sedimentation analysis of the association of various BacA variants with liposomes.** The indicated proteins (20 µM)
925 were incubated without (-) or with (+) liposomes (0.4 mg/mL) prior to ultracentrifugation. The supernatant (S) and pellet (P)
926 fractions of each mixture were analyzed by SDS gel electrophoresis. Shown are scans of representative gels and a quantification
927 of the average amount of protein (± SD) contained in the different fractions (n=3 independent replicates).

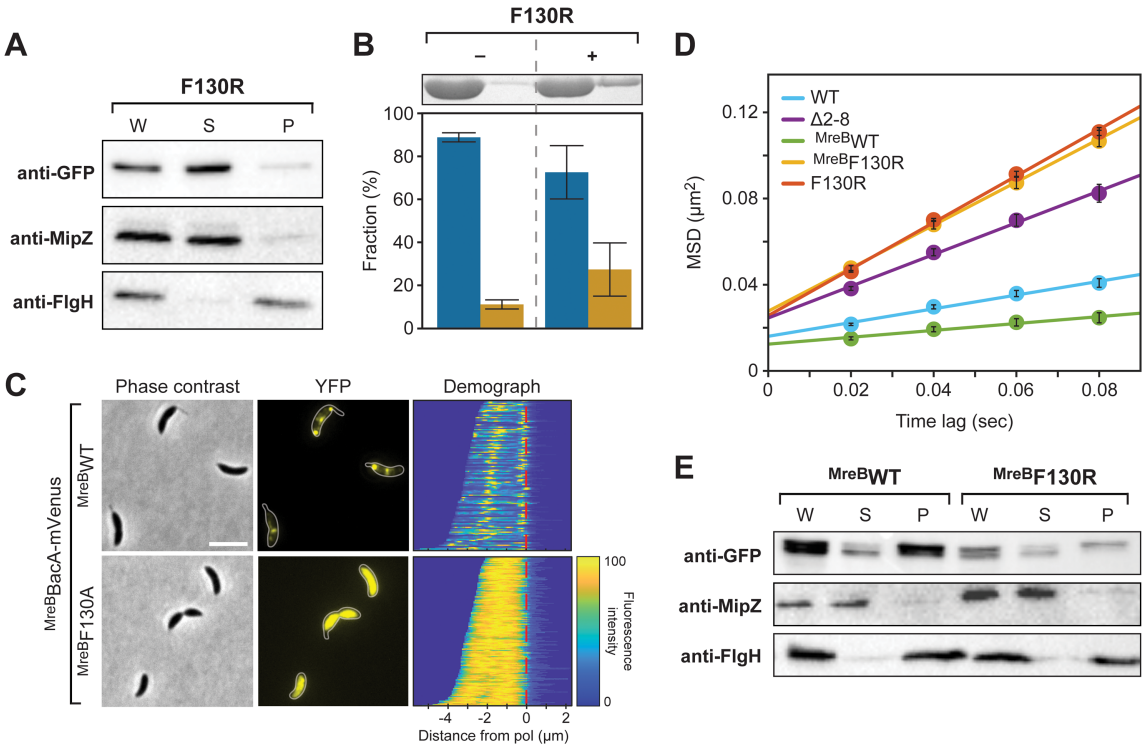

928 **Figure 4. Interdependence of BacA polymerization and membrane binding. (A)** Cell fractionation experiment investigating the
929 membrane-binding activity of the polymerization-deficient F130R variant of BacA-mVenus *in vivo* (LY119). The analysis was
930 performed as described for **Figure 2B**. **(B)** Co-sedimentation analysis of the association of BacA-F130R with liposomes *in vitro*,
931 performed as described for **Figure 3**. **(C)** Role of polymerization in the membrane association of a BacA-mVenus variant carrying
932 the membrane-targeting sequence of *E. coli* MreB. Shown are phase contrast and fluorescence images of Δ*bacAB* mutants (LY103,
933 LY123) producing either a BacA-mVenus variant in which the MTS is replaced by two tandem copies of the N-terminal amphiphilic
934 helix of *E. coli* MreB (^{MreB}WT) or a polymerization-deficient variant thereof (^{MreB}F130A). Demographs summarizing the single-cell
935 fluorescence profiles obtained from random subpopulations of cells are given next to the respective fluorescence images. The
936 numbers of cells analyzed are: ^{MreB}WT (126), ^{MreB}F130A (169). The vertical red line indicates the junction between cell body and
937 the stalk. Scale bar: 1 µm. **(D)** Mobility of the indicated BacA-mVenus fusion proteins. Shown is the average mean-squared dis-
938 placement (MSD) (± SD) as a function of time, based on single-particle tracking analysis. **(E)** Cell fractionation experiment in-
939 vestigating the membrane-binding activity of ^{MreB}BacA-mVenus (^{MreB}WT) and its polymerization-deficient F130R variant
940 (^{MreB}F130R) *in vivo* (LY103, LY123). The analysis was performed as described for **Figure 2B.**

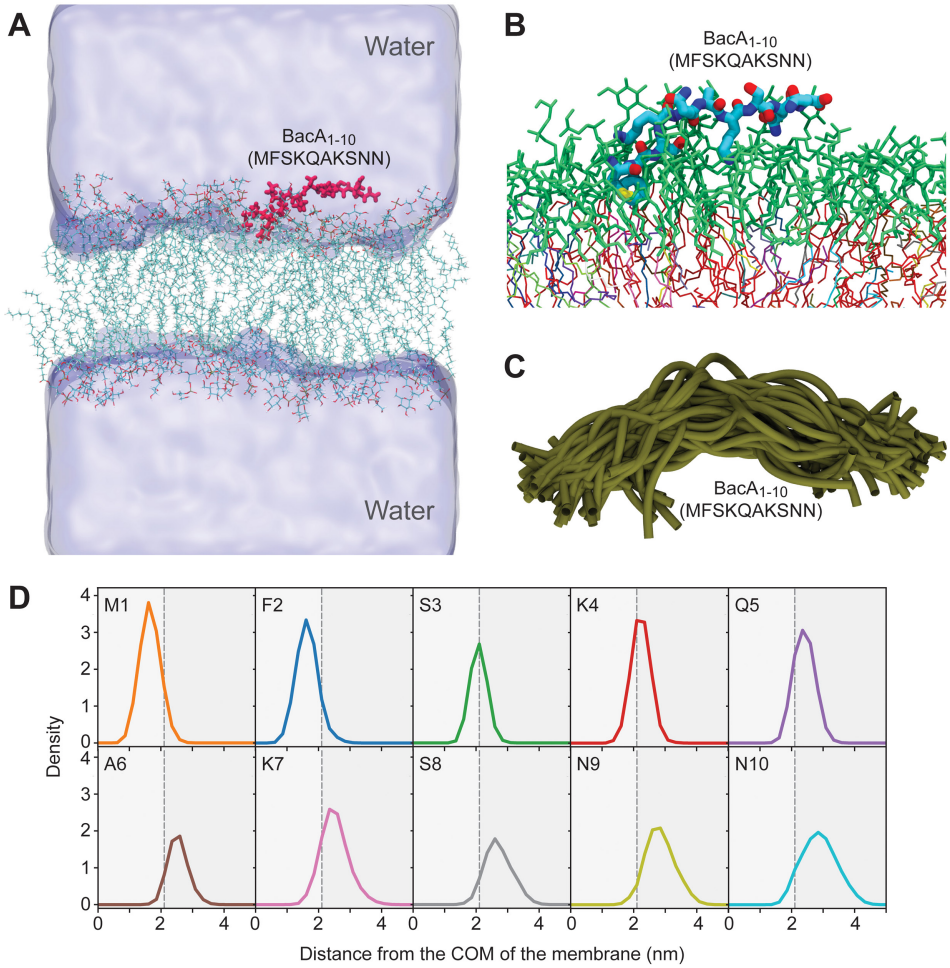

Figure 5. Molecular dynamics simulation of the interaction between the BacA MTS and a model membrane. (A) Snapshot of the molecular dynamics (MD) simulation system showing the 10-mer peptide MFSKQAKSNN ($BacA_{1-10}$; red) after binding to the lipid bilayer. The water is shown in surface representation. K^+ and Cl^- counterions are not shown. **(B)** Close-up view of a representative snapshot from the MD simulation visualizing the binding mode of the peptide on the membrane surface. **(C)** Structural overlay of 40 snapshots from the MD simulation, taken after constant time intervals from the trajectory. **(D)** Density profiles of individual residues in the wild-type peptide along the membrane normal, i.e. the z-component of the distance vector from the center-of-mass (COM) of the bilayer, with the membrane midplane located at zero. The vertical dashed black line indicates the maximum of the density distribution of the lipid headgroup phosphates.

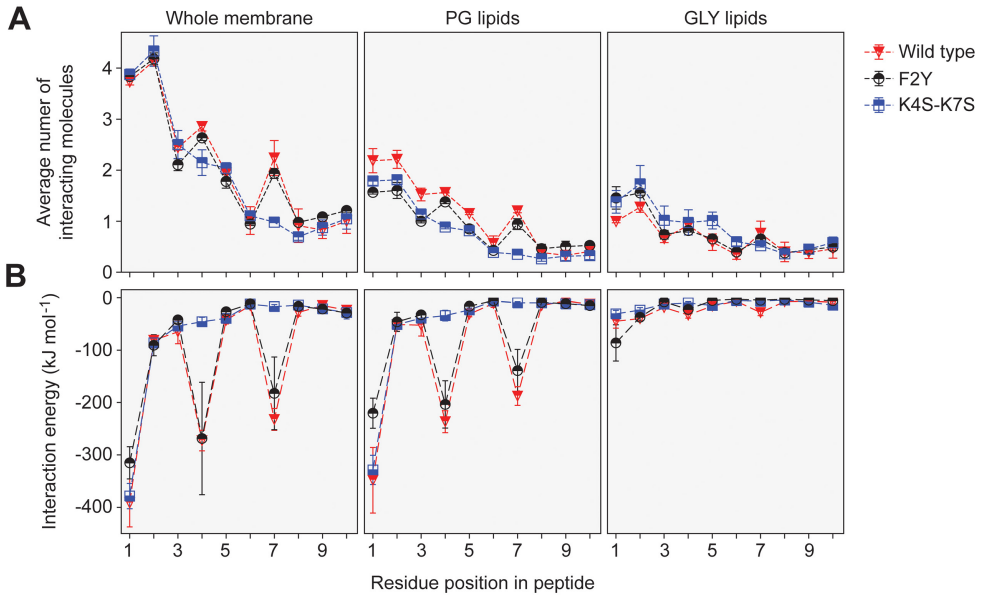

Figure 6. Contact numbers and interaction energies for different peptide-lipid bilayer interactions. (A) The graph shows the total number of contacts between individual residues in the wild-type, K4S-K7S and F2Y peptides and the lipid bilayer as well as the number of contacts with PG lipids and GLY lipids. A contact between a peptide residue and a lipid was defined to exist if any two non-hydrogen atoms of the residue and a lipid molecule were within a distance of 0.5 nm to each other. Contacts were counted for each frame of the MD trajectories and averaged. Multiple contacts between a peptide and a lipid molecule were treated as a single contact, so that the number of contacts counted was either 1 or 0. The statistical errors plotted were obtained from the difference between the two different sets of 500-ns simulations, starting with peptides in an unfolded or α-helical conformation, respectively. **(B)** Energies of the interactions between individual residues in the wild-type, K4S-K7S and F2Y peptides and the lipid bilayer. The interaction energies plotted are the combined interaction energies of all Coulomb and van-der-Waals interactions in the force field averaged over the simulation trajectories.

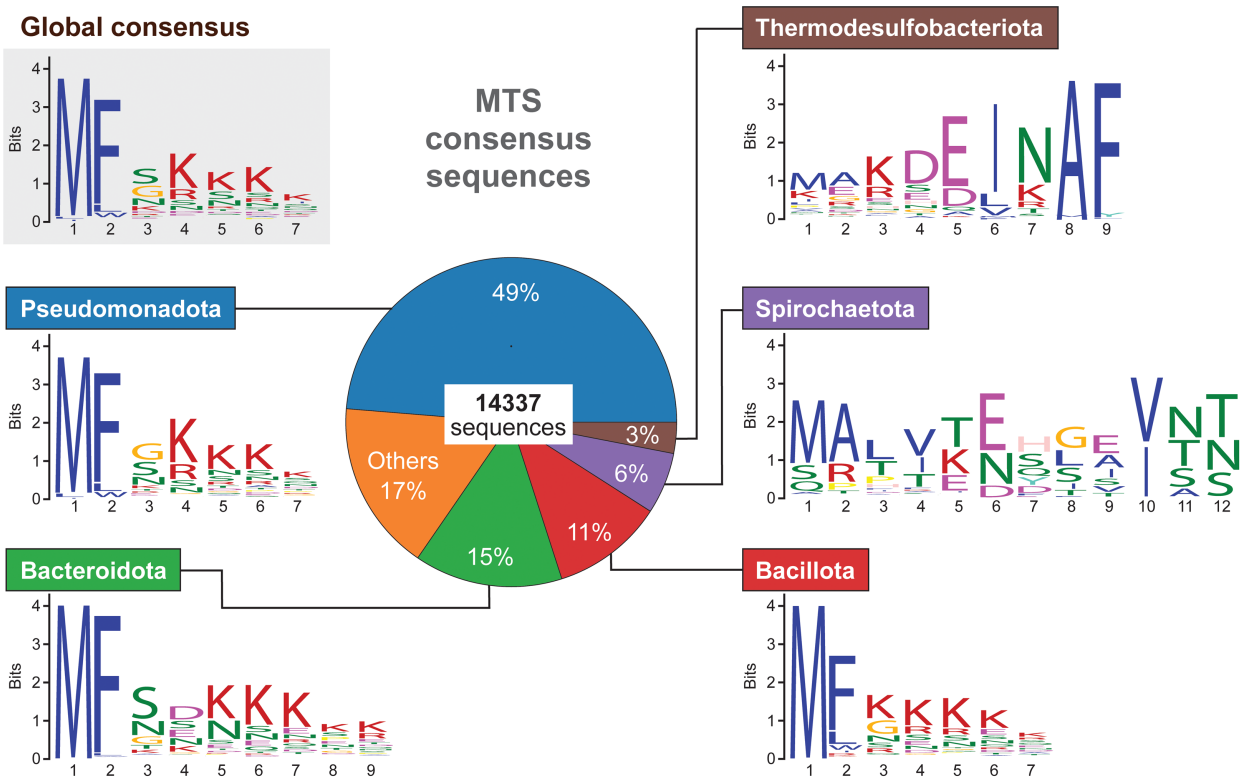

Figure 7. Conservation of the N-terminal regions of bactofilin homologs in different bacterial phyla. The pie chart in the middle shows the relative distribution of the 14337 unique bactofilin homologs analyzed among the indicated bacterial phyla. The sequence logos give the the most widespread N-terminal motifs obtained either by a global analysis of all 14337 bactofilin sequences (global consensus) or by an analysis of subsets of these sequences from specific phyla.

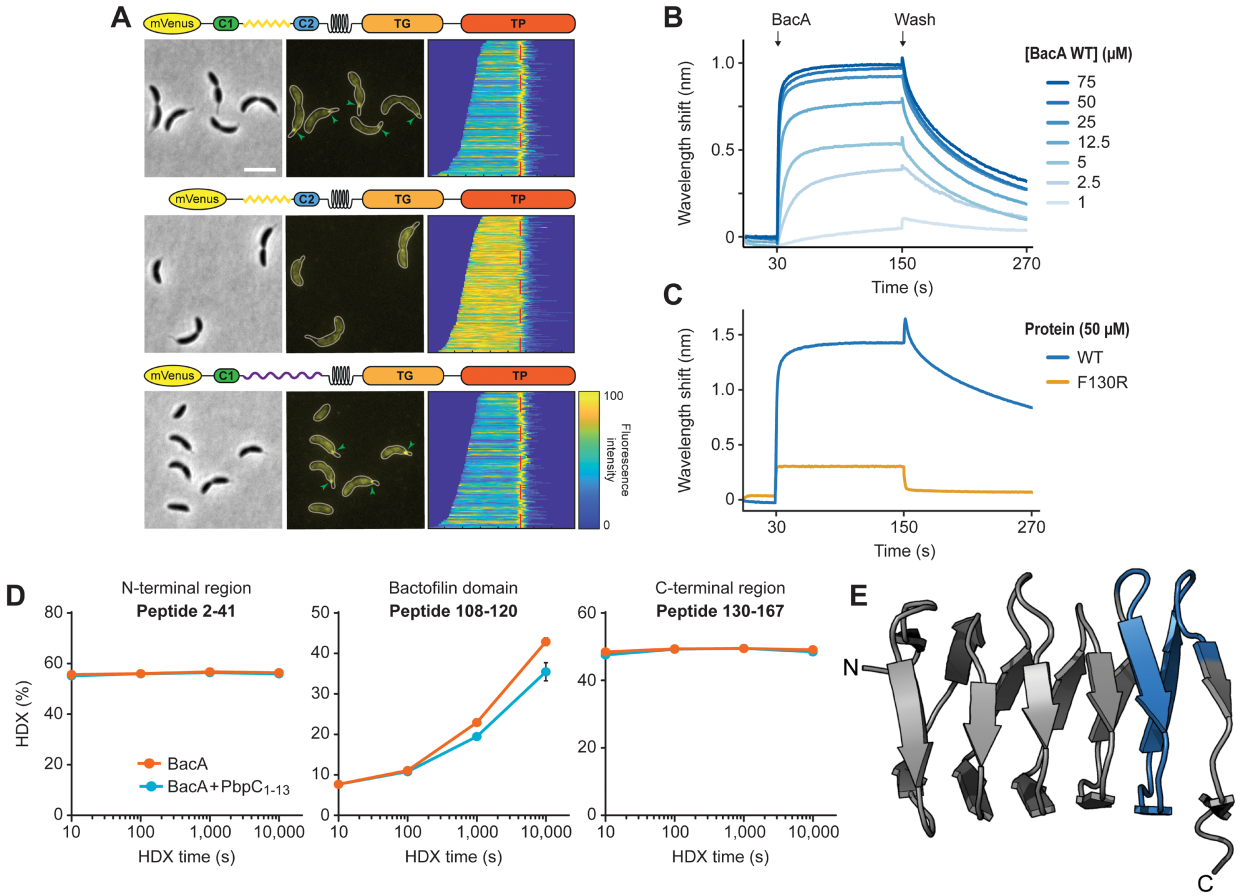

Figure 8. Interaction of BacA with its client protein PbpC. (A) Localization patterns of different PbpC variants. Δ*bacB* Δ*pbpC* cells producing mVenus-PbpC (LY75) or mutant variants thereof lacking region C1 (LY76) or carrying an unstructured region from *C. crescentus* DipM in place of the unstructured region connecting region C1 and the transmembrane helix (LY77) were analyzed by phase contrast and fluorescence microscopy. The outlines of the cells are shown in the fluorescence images. Demographs summarizing the single-cell fluorescence profiles obtained from random subpopulations of cells are given next to the respective fluorescence images. The numbers of cells analyzed are: LY75 (158), LY76 (253), LY77 (119). Scale bar: 1 µm. **(B)** Biolayer interferometric analysis of the interaction between $PbpC_{1\text{-}13aa}$ and BacA. A synthetic peptide comprising the first 13 amino acids of PbpC ($PbpC_{aa1\text{-}13}$) was immobilized on a biosensor and probed with increasing concentrations of BacA. After the association step, the sensor was transferred to a protein-free buffer to monitor the dissociation reaction. The graph shows a representative titration series (n=3 independent replicates). **(C)** Comparison of the interaction of $PbpC_{aa1\text{-}13}$ with BacA and its polymerization deficient F130R variant, performed as described in panel B. **(D)** Mapping of the PbpC binding site on BacA by hydrogen-deuterium exchange (HDX) mass spectrometry. The plots show the extent of deuterium uptake by three representative peptides obtained after tryptic digestion of BacA protein (2.5 µM) that had been incubated in the absence or presence of $PbpC_{aa1\text{-}13}$ peptide (10 µM) for the indicated time periods (see **Data S1** for the full set of peptides). **(E)** Mapping of the the differences in deuterium uptake observed at t=1000 s onto the solid-state NMR structure of BacA (Shi et al., 2015).